C2FUEL - This project has received funding from the European Union's Horizon 2020
research and innovation programme under grant agreement No 838014
The C2FUEL project results presented reflect only the author's view.
The Commission is not responsible for any use that may be made of the information it contains.

C2FUEL

Carbon Captured Fuel and Energy Carriers for an Intensified Steel Off-Gases based Electricity Generation in a Smarter Industrial Ecosystem

Deliverable

D2.7 Multiscale modelling results

WP2 – High temperature electrolysis development

Project information

Grant Agreement n°	838014
Dates	1st June 2019 – 30th November 2023

Document Status

Document information

Deliverable name	Multiscale modelling results
Responsible beneficiary	XIUFU SUN / DTU
Contributing beneficiaries	Timo Lehtinen / ELCOGEN
Contractual delivery date	M32 –30/01/2022
Actual delivery date	M39 – 24/08/2022
Dissemination level	Public

Document approval

Name	Position in project	Organisation	Date	Visa
P. OLIVIER	Coordinator	ENGIE	01/08/2022	OK
L. NAIGLIN	Project Management Officer	AYMING	24/08/2022	OK
A. MIQUELOT	Project Management Officer	ENGIE	01/08/2022	OK
M.NOPONEN	WP2 LEADER	ELCOGEN	06/07/2022	OK

Document history

Version	Date	Modifications	Authors
V1	09/06/2022	1ST DRAFT	Xiufu Sun / DTU
V2	06/07/2022	Second version	Xiufu Sun / DTU
V3	01/08/2022	Third version	Adeline Miquelot / ENGIE
VF	24/08/2022	Final version	Laurence Naiglin / BENKEI

Table of Contents

List of Figures

List of Tables

Deliverable report

1 Executive Summary

1.1 Description of the deliverable content and purpose

This deliverable deals with detailed 3D and 1D/0D modelling of [**ELCOGEN**] cells and stacks.

1.2 Brief description of the state of the art and the innovation breakthroughs

Numerical modeling of SOEC stacks is computationally expensive since it requires a multiphysics approach to model interactions of various physics at different layers. Thus, a detailed 30-cell stack stationary run with a conventional rectangular flow field design takes about 40 hours [1]. Considering coupling and interrelations of transport equations of mass, momentum, species, charges, and heat at different layers of a single cell or repeating unit makes their 3D simulations computationally expensive. Therefore, 3D models with simplifying assumptions such as isothermal have been developed, or detailed multiphysics models have been applied to the 1D and 2D models. The models at the cell and repeating unit scales are not good representatives of the stack performance as the variations of the modeling variables along the height of the stack are missed in these models. In our recent studies [2-4], we have been using a homogenization approach to make the stack-scale simulations of SOECs feasible on typical computational workstations.

1.3 Corrective action (if relevant)

In the description of action, "0D and 3D stack modelling will be carried out to understand the SOE stack behaviour under steady state operation as well as dynamic operation conditions with special focus on the heat management and carbon formation prediction during co-electrolysis operation". However, based on the stack test results, accelerated degradation on one of the repeating units was observed, it is speculated that the operation condition/operation history may create mechanical stress on the stack, which eventually caused the loss of contact area of the repeating unit. Therefore, instead of modelling of carbon deposition in co-electrolysis operation, large efforts were made on mechanical modelling in order to understand the cause of the stress and provide input for the stack design for final demonstration.

Moreover, although the initial plan of modelling of 15 cells stack (stacks tested at [**DTU**]), additional modelling efforts have also been devoted to simulate the 39 cells large stack which will be used for final demonstration.

The obtention of all these modelling data has created a delay in the delivery of this report.

1.4 IPR issues (if relevant)

Not applicable.

2 Introduction

Multiscale modelling of SOEC stacks provides insight in flow, species transport / conversion, current distribution, heat distribution during SOEC steady-state and dynamic operation. In this task, 0D and 3D stack modelling will be carried out to understand the SOE stack behaviour under steady state operation (at constant current) as well as dynamic operation conditions (at different currents) with special focus on the heat management and stress distribution.

3 3D stack multiphysics electrochemical modeling

A multiphysics model including transport equations of mass, momentum, species, charges, and heat is used. This model has been developed and presented in [DTU]'s previous works [2-4]. In the model, a homogenization approach is applied to the layered domains of the stack, which solves for the effective modeling variables over an equivalent porous domain with effective modeling parameters and properties for each physics. The application of this approach to the active area of the stack was introduced in [2]. The additions of the headers, sealing, and manifolds to the model are presented in [3,4]. The 3D schematic of the modeling domain used for the {ELCOGEN] stacks is shown in Figure 1.

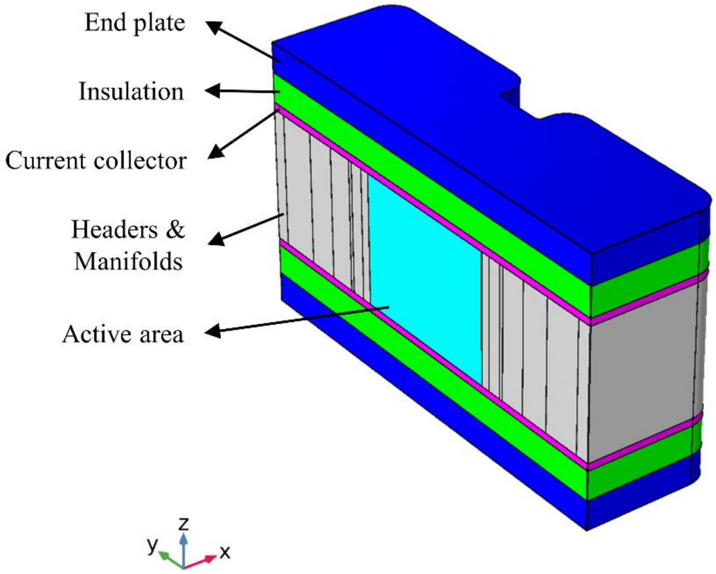

Figure 1: Schematic of the stack configuration. The modeling domain is the right half of the stack with symmetry boundary condition on the middle surface in the x-direction

The homogenization approach that has been used in this stack-scale model is like the homogenization used for the electrodes of a single cell, in which the transport equations are solved over an equivalent domain with effective modeling variables instead of solving the equations on a detailed electrode geometry with all the phases and pores. The homogenized stack model replaces the whole repeating unit with an equivalent domain. This approach has been used by several research groups, e.g. in [5] for an SOFC stack and [6] for a polymer electrolyte fuel cell stack, and European companies. In our recent work [3], we validated our stack-scale model against the experimental data for the 18-cell FZJ Mark-F SOFC stack [7] under stationary operation.

The transport governing equations that are solved at the stack scale to obtain the effective modeling variables are given in Table 1, and the cell model equations used to evaluate the polarization characteristics of the cells are listed in Table 2.

Table 1: Governing equations for the homogenized stack model

Description	Transport equation	Eq. #
Mass	$\nabla \cdot (\rho \mathbf{u}) = S_{\mathrm{m}}$	(1)
Momentum	Darcy's Law (homogenized domains): $\nabla p = \frac{\mu}{K} u_{av}$ Navier-Stokes (manifolds): $\rho(\mathbf{u}.\nabla)\mathbf{u} = -\nabla p + \mu \nabla^2 \mathbf{u}$	(2)
Species	$\nabla \cdot \left(-\rho w_{\mathrm{i}} \sum_j D_{\mathrm{ij}} \nabla w_{\mathrm{j}} \right) + \rho(\mathbf{u} \cdot \nabla) w_{\mathrm{i}} = S_{\mathrm{i}}$	(3)
Heat	$(\rho c_p)_{\mathrm{eff}} \mathbf{u} \cdot \nabla T + \nabla \cdot (-k_{\mathrm{eff}} \nabla T) = S_{\mathrm{T}}$	(4)
Charge	$\nabla \cdot (-\sigma \nabla V + J_e) = S_{\mathrm{j}}$	(5)

Table 2: Cell model equations

Description	Governing equation	Eq. #
Cell voltage [2]	$V_{cell} = E - \eta_{act,an} - \eta_{act,ca} - \eta_{conc,an} - \eta_{conc,ca} - \eta_{ohm}$	(6)
OCV [2]	$E = \frac{\Delta G_{rx,H_2O}}{2F} + \frac{RT}{2F}\ln\left(\frac{p_{H_2}p_{O_2}^{1/2}}{p_{H_2O}p_0^{1/2}}\right)$	(7)
BV for the anode reaction rate [8]	$i_{\mathrm{an}} = i_{0,\mathrm{an}}\lambda_{\mathrm{an,eff}}\left[\exp\left(\frac{2F}{RT}\,\eta_{\mathrm{act,an}}\right) - \exp\left(-\frac{F}{RT}\,\eta_{\mathrm{act,an}}\right)\right]$	(8)
BV for the cathode reaction rate [9]	$i_{\mathrm{ca}} = i_{0,\mathrm{ca}}\lambda_{\mathrm{ca}}\left[\exp\left(\frac{2F}{RT}\,\eta_{\mathrm{act,ca}}\right) - \exp\left(-\frac{2F}{RT}\,\eta_{\mathrm{act,ca}}\right)\right]$	(9)
Anode exchange current density [10]	$i_{0,\mathrm{an}} = 31.4\, p_{\mathrm{H_2}}^{-0.03}\, p_{\mathrm{H_2O}}^{0.4} \exp\left(-\frac{18300}{T}\right)$	(10)
Cathode exchange current density [11]	$i_{0,\mathrm{ca}} = 2.14 \times 10^5\, p_{\mathrm{O_2}}^{0.376}\, \exp\left(-\frac{29200}{T}\right)$	(11)
Anode concentration overpotential [12]	$\eta_{conc,an} = \frac{RT}{2F}\ln\left(\frac{1 + \frac{RTh_{an}}{2FD_{H_2O}^{eff}p_{H_2O}}j}{1 - \frac{RTL_{an}}{2FD_{H_2}^{eff}p_{H_2}}j}\right)$	(12)
Cathode concentration overpotential [12]	$\eta_{conc,ca} = \frac{RT}{4F}\ln\left(\frac{1}{1 - \frac{RTh_{ca}}{4FD_{O_2}^{eff}p_{O_2}}j}\right)$	(13)
Ohmic overpotential [13]	$\eta_{ohm} = \frac{h_i}{\sigma_i}j\,;\ \begin{cases} \sigma_{Ni} = 3.27 \times 10^6 - 1065.3T \\ \sigma_{LSM} = \frac{4.2 \times 10^7}{T}\exp\left(-\frac{1150}{T}\right) \\ \sigma_{YSZ} = 6.25 \times 10^4 \exp\left(-\frac{10300}{T}\right) \end{cases}$	(14)

3.1 Fuel cell operation mode

This section presents the modeling results for the 15- and 39-cell stacks under the fuel cell operation mode. The operating conditions are listed in Table 3.

Table 3: Operating conditions for the 15- and 39-cell stacks under the SOFC operation mode

Parameter	Value, 15-cell stack	Value, 39-cell stack	Description
p_{op}	1 atm	1 atm	Operating pressure
T_{in}	703.5 °C	613 °C	Inflow temperature
$T_{furnace}$	703.5 °C	613 °C	Furnace temperature
$Q_{in,fuel}$	15.5 nlpm	40 nlpm	Fuel inlet flow rate
$Q_{in,air}$	33 nlpm	86 nlpm	Air inlet flow rate
$x_{H_2,in}$	0.494	0.498	Hydrogen mole fraction at the fuel inlet
$x_{N_2,in,fuel}$	0.5	0.5	Nitrogen mole fraction at the fuel inlet
$x_{O_2,in}$	0.21	0.21	Oxygen mole fraction at the air inlet

3.1.1 Model validation

Figure 2 shows the comparisons of the polarization curves and temperatures at the center of the stack from the experimental data and simulations for the 15- and 39-cell stacks under fuel cell operation mode. A good match is seen for the polarization curves (IVs), which is done through a correcting coefficient for the triple phase boundaries (TPBs) of the anode and cathode electrodes. This modification is necessary to match the experimental and simulated IVs since the cell parameters are from the literature(see references given in Table 2), which would be different for the [**ELCOGEN**] cells used in these stacks.

Under the fuel cell operation mode, the overall reaction is exothermic, and so its heat source adds up with the ohmic heat sources from the overpotentials. Therefore, a monotonous increase in temperature with the load current is expected for the SOFC operation mode, as shown in Figure 2. The model predicts the temperature evolution with the load current as well, but there are deviations between the experimental and simulation values. The reason for such differences would be the simplifications used in the homogenized stack model. However, there are other reasons such as: 1) the furnace temperature is fixed in the simulations since during the stack testing phase the furnace setting point was fixed. and 2) a steady state is considered for each operating load current in simulations while the experimental data do not show a stationary operation (especially at the beginning for lower load currents) due to a high load current rate of 1 A/min used in the experiments, which could lead to delay in temperature change due to the low heat transfer rate compared with the current ramp rate. As an additional information, in real conditions we can lower the temperature of the furnace to maintain the same temperature as the setting point, in the experiments under the SOFC operation mode, to counteract the exothermicity of the reaction.

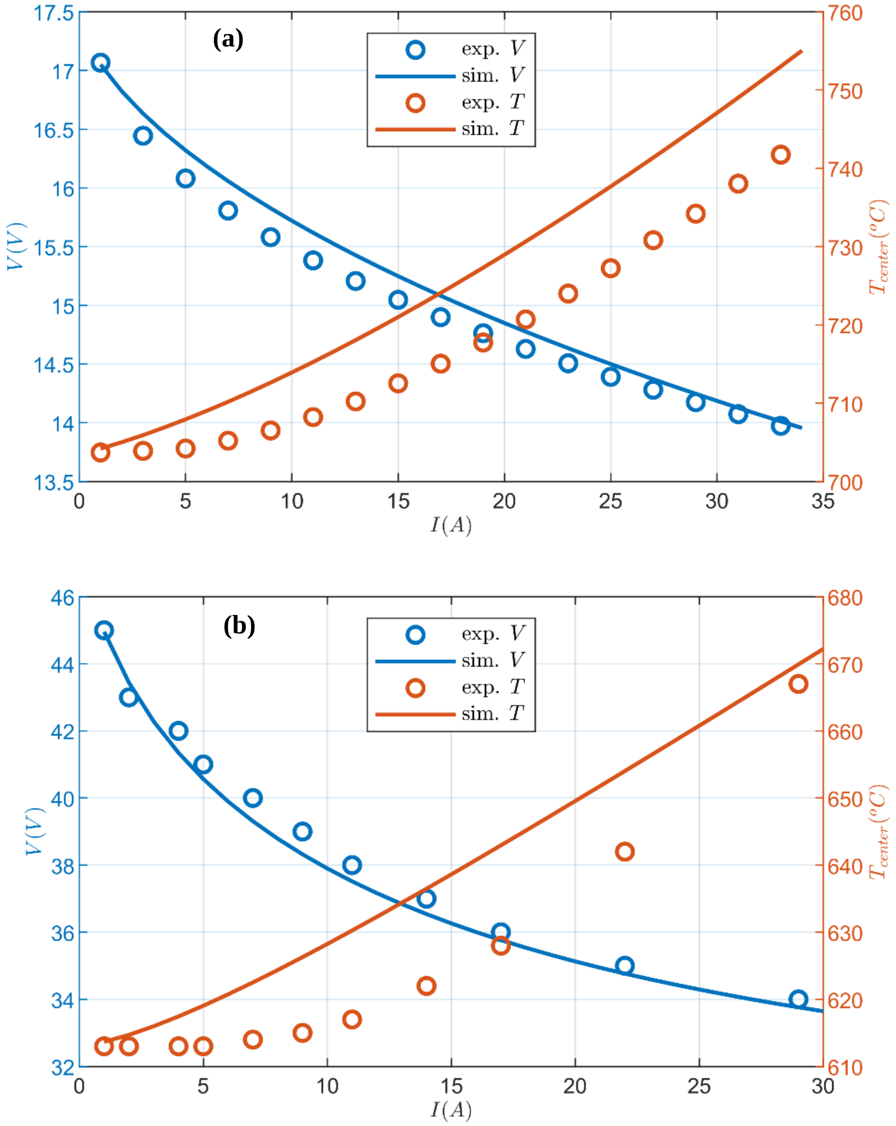

Figure 2: Comparisons of the polarization curves and temperatures at the center of the stack from the experimental data and simulations for (a) 15-cell stack and (b) 39-cell stack under fuel cell operation mode

3.1.2 Species distribution

Figure 3 shows the distributions of the hydrogen mole fraction for the 15- and 39-cell stacks at the load current of 30 A. The hydrogen mole fraction drops from the inlet, at the front of the stack, to the outlet, at the back of the stack, due to the hydrogen consumption over the active area under the SOFC operation mode. Since the effective fuel flow rate per cell is almost the same for both stacks, as given in Table 3, their minimum hydrogen mole fraction is very close. Moreover, it should be noted that thanks to the novel header design in these stacks, the hydrogen mole fraction is almost uniform across the stack in the x-direction.

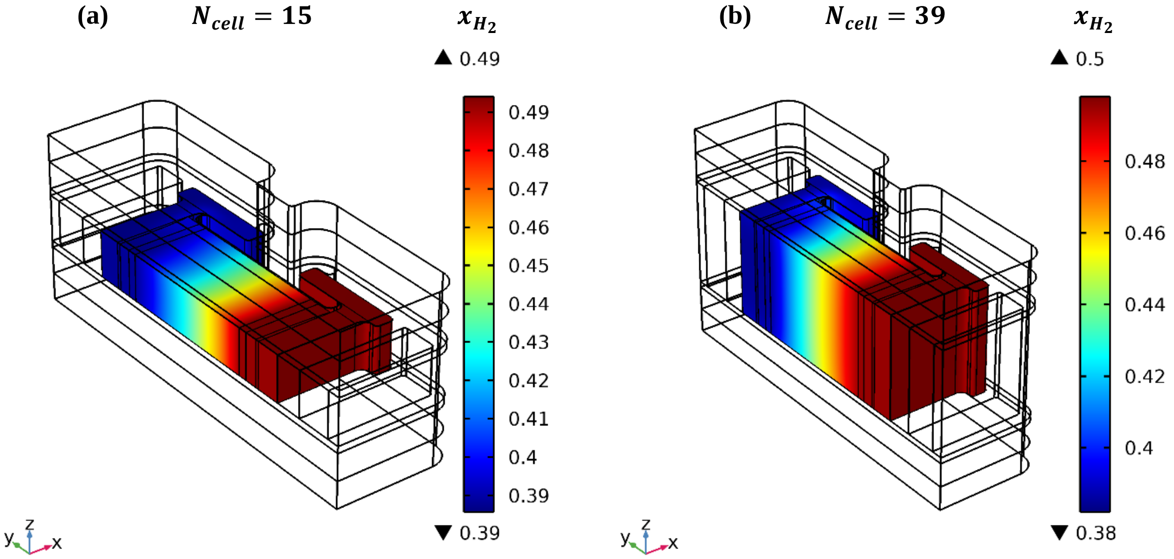

Figure 3: Distributions of the hydrogen mole fraction for (a) 15-cell stack and (b) 39-cell stack at the load current of 30 A

Figure 4 shows the distributions of the oxygen mole fraction for the 15- and 39-cell stacks at the load current of 30 A. The oxygen mole fraction drops from the inlet, at the front of the stack, to the outlet, at the back of the stack, due to the oxygen consumption over the active area under the SOFC operation mode. Since the effective air flow rate per cell is almost the same for both stacks, as given in Table 3, their minimum oxygen mole fraction is very close. Moreover, it should be noted that thanks to the novel header design in these stacks, the oxygen mole fraction is almost uniform across the stack in the x-direction. Nonetheless, the side air channel between the active area and the side part, which is used for better heat transfer inside the stack, leads to an air flow skipping the active area and flowing directly from the inlet to the outlet.

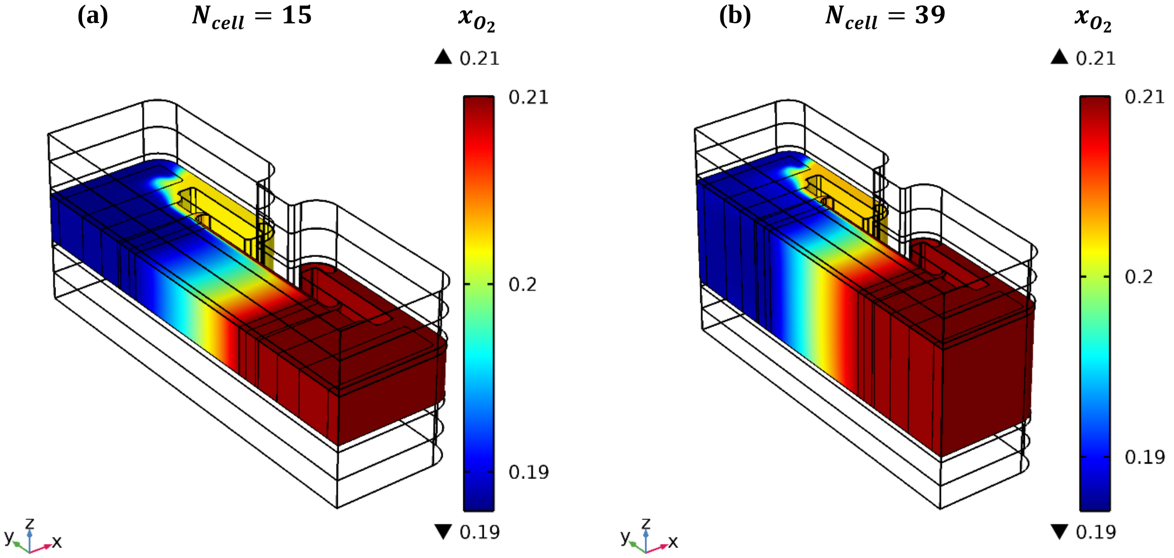

Figure 4: Distributions of the oxygen mole fraction for (a) 15-cell stack and (b) 39-cell stack at the load current of 30 A

3.1.3 Temperature distribution

Figure 5 shows the distributions of the temperature over the whole stack for the 15- and 39-cell stacks at the load current of 30 A. As mentioned in Section 3.1.1, the heat sources from the overall reaction and overpotentials add up under the SOFC operation mode, resulting in a temperature increase from the inlet to the outlet. It should be mentioned that the thermal boundary conditions over the outer boundaries of the stacks are defined as radiation with ambient at the furnace temperature and convection with air at the furnace temperature. This is why the temperature is not uniform over the outer boundaries of the stacks and is a bit higher for the current collectors' boundaries. A higher temperature increase is seen for the 39-cell stack than for the 15-cell stack, while the effective fuel and air flow rates per cell are almost the same for both stacks. The reason is the lower temperature level for the 39-cell stack, which leads to higher overpotentials and so enhances their corresponding heat sources.

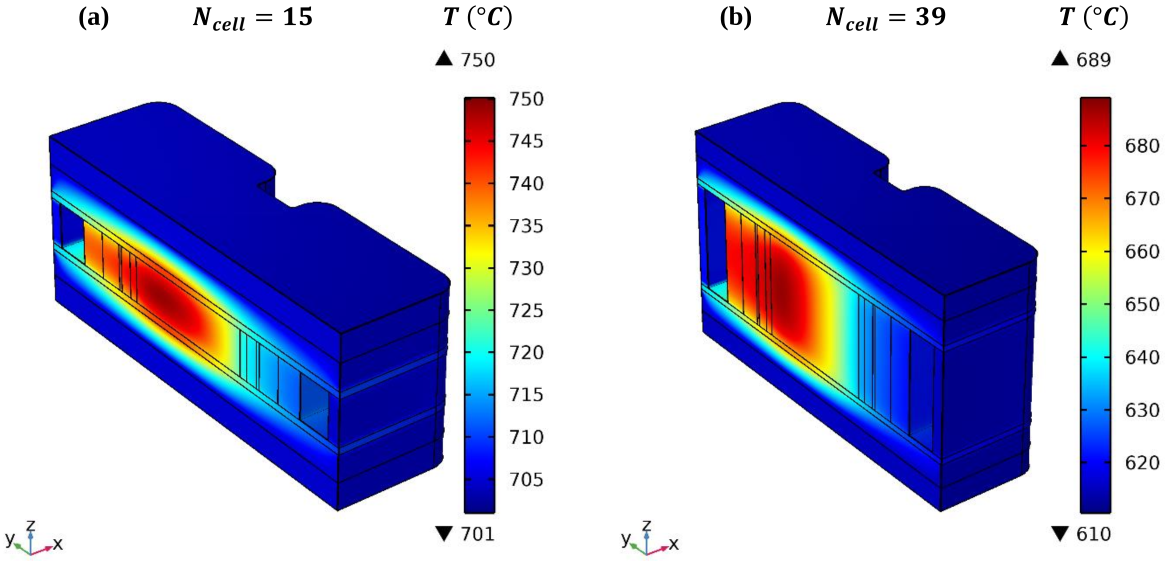

Figure 5: Distributions of the temperature for (a) 15-cell stack and (b) 39-cell stack at the load current of 30 A

3.1.4 ASR distribution

Figure 6 shows the distributions of the area specific resistance (ASR) for the 15- and 39-cell stacks at the load current of 30 A. The ASR is higher/lower at the inlet/outlet of the active area due to lower/higher temperatures at the inlet and outlet, respectively, as shown in Figure 5. Moreover, a higher ASR level is seen for the 39-cell stack compared to the 15-cell stack due to its lower temperature level.

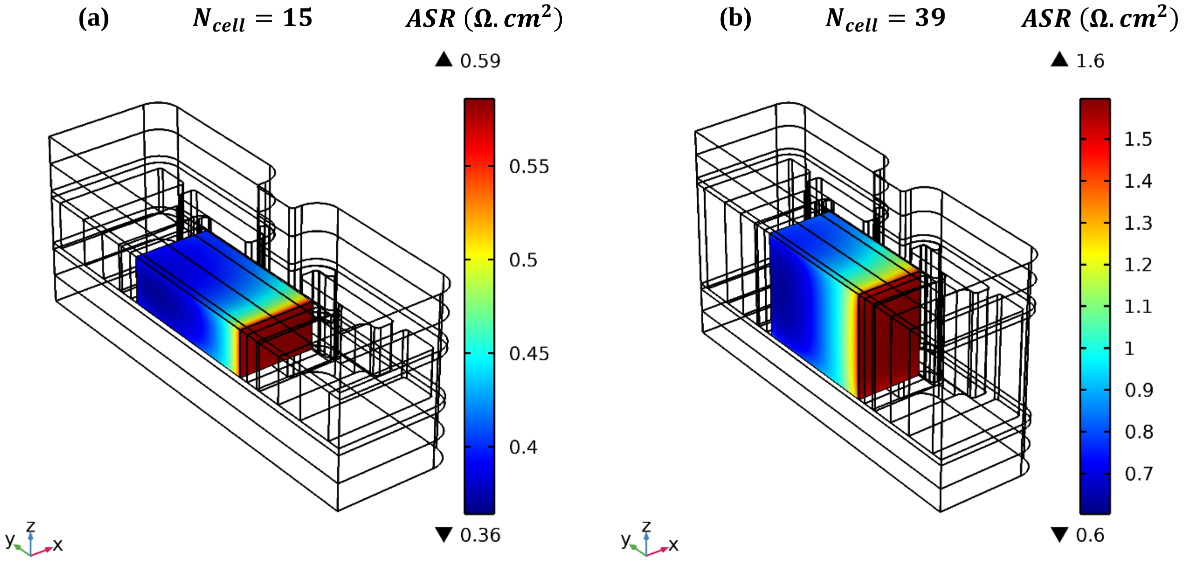

Figure 6: Distributions of the ASR for (a) 15-cell stack and (b) 39-cell stack at the load current of 30 A

3.1.5 Current density distribution

Figure 7 shows the distributions of the current density for the 15- and 39-cell stacks at the load current of 30 A. For the 15-cell stack, the common trend of maximum/minimum current densities at the inlet/outlet of the active area is seen. However, for the 39-cell stack, the maximum current density is shifted to the outlet of the active area due to the dominant effect of the higher ASR for this stack. In addition, the higher ASR level for the 39-cell stack makes its current density distribution more uniform compared to the 15-cell stack. Nonetheless, for higher load currents with higher drops in the hydrogen concentration over the active area, the concentration effect gets dominant over the ASR, and so the current density distribution changes to the expected trend with the maximum at the inlet of the active area, as shown in Figure 8 for the load current of 131 A.

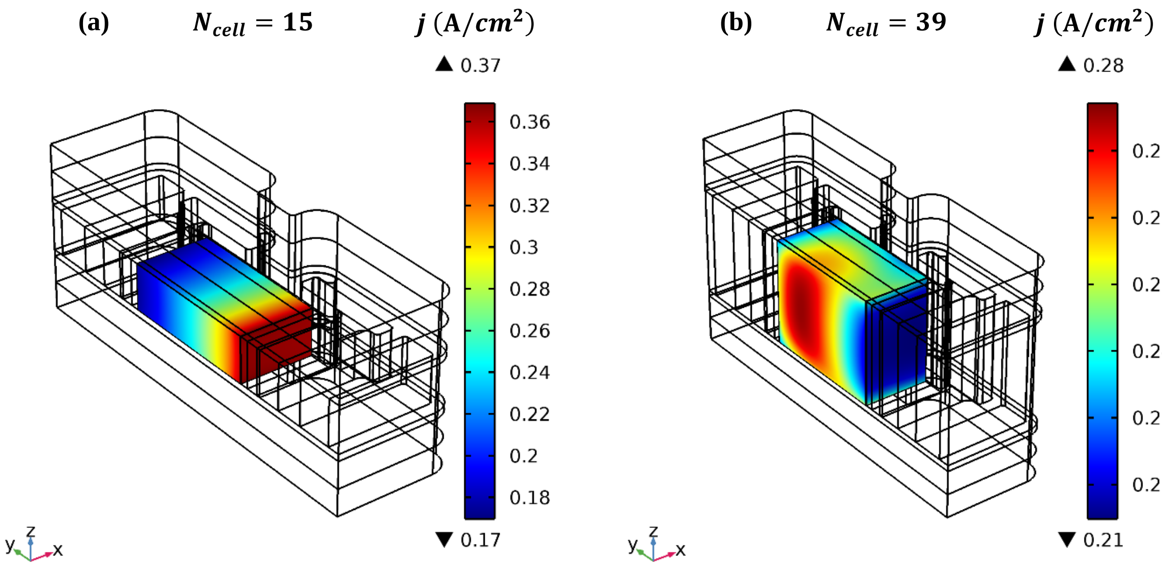

Figure 7: Distributions of the current density for (a) 15-cell stack and (b) 39-cell stack at the load current of 30 A

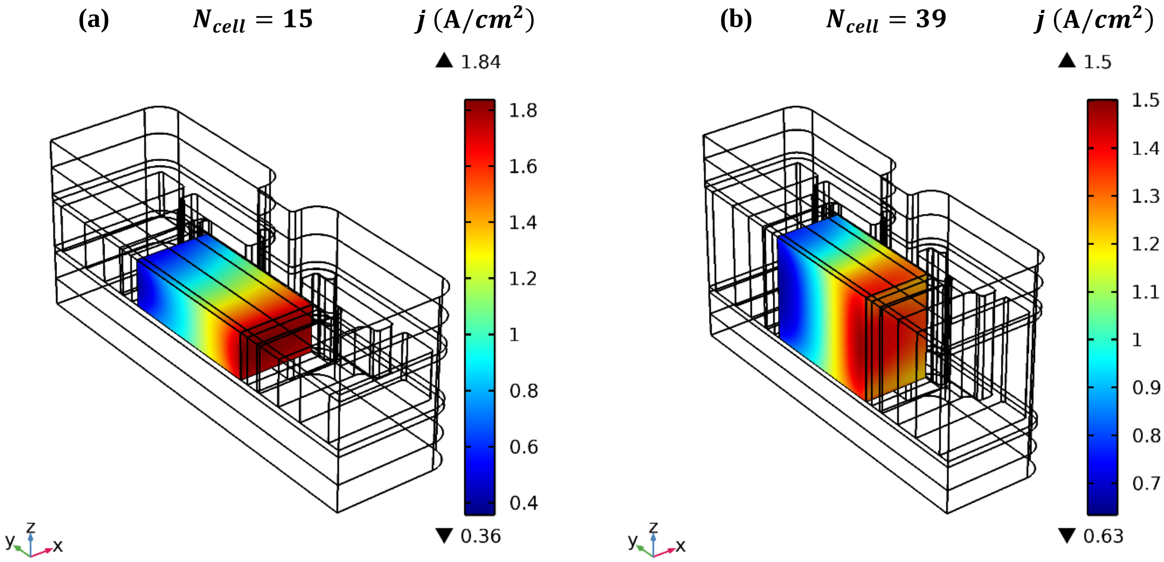

Figure 8: Distributions of the current density for (a) 15-cell stack and (b) 39-cell stack at the load current of 131 A

3.1.6 Pressure distribution

Figure 9 shows the distributions of the air and fuel pressures for the 15- and 39-cell stacks at the load current of 30 A. The flow boundary conditions are defined as the flow rate at the inlet, values given in Table 3, and the outlet pressure is set to atmospheric pressure. It needs to be mentioned that the color bars show the gauge pressure. Therefore, the maximum pressures at the inlets show the pressure drops along the stack for each flow field. Again, thanks to the novel header design in these stacks, the pressures are almost uniform across the stacks in the x-direction.

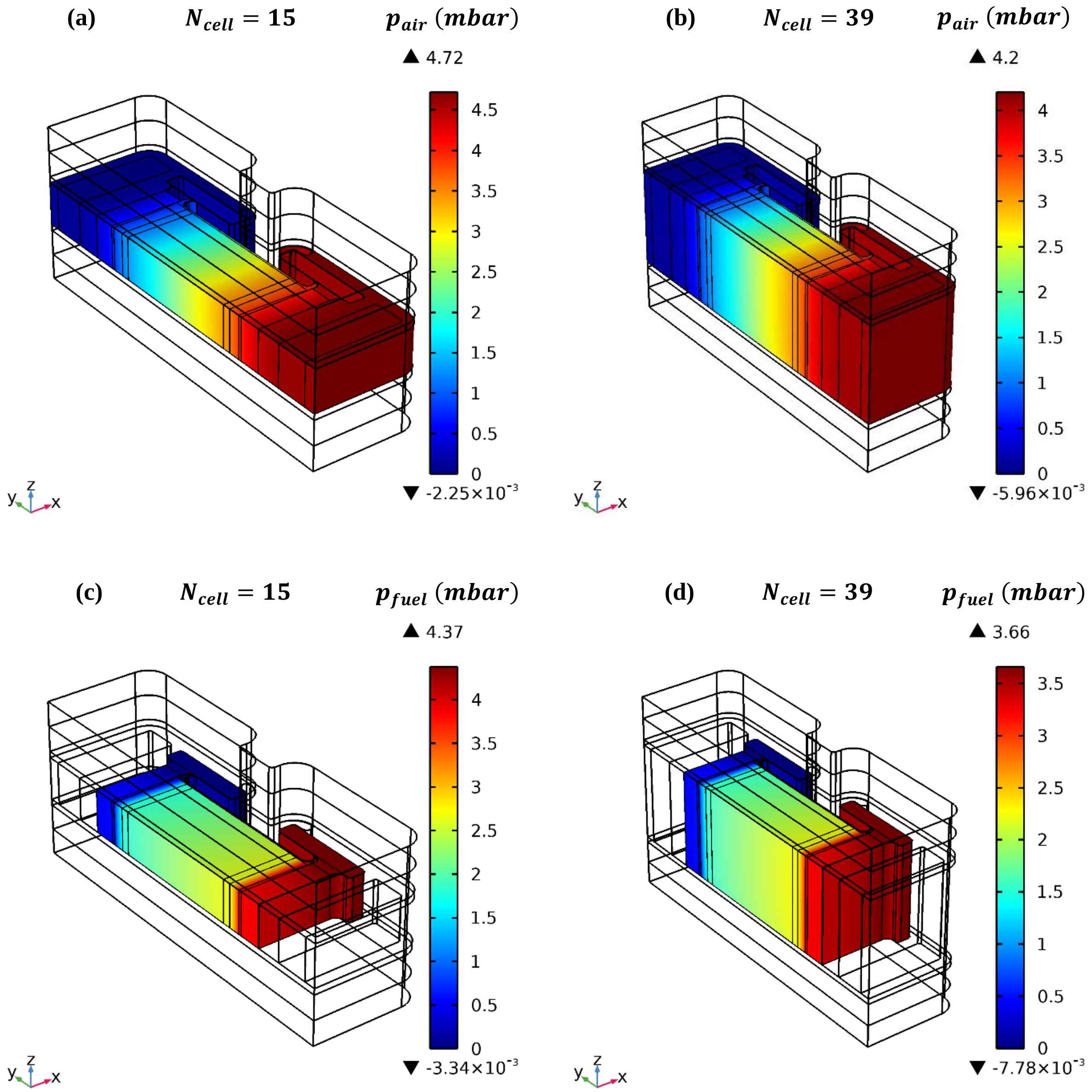

Figure 9: Distributions of the air and fuel pressures for the 15-cell stack, (a) and (c), and 39-cell stack, (b) and (d), at the load current of 30 A. The color bars show the gauge pressure values.

3.2 Electrolysis operation mode

This section presents the modeling results for the 15-cell stack under the electrolysis operation mode. The operating conditions are listed in Table 4.

Table 4: Operating conditions for the 15-cell stack under the SOEC operation mode

Parameter	Value, 15-cell stack	Description
p_{op}	1 atm	Operating pressure
T_{in}	699 °C	Inflow temperature
$T_{furnace}$	699 °C	Furnace temperature
$Q_{in,fuel}$	11.72 nlpm	Fuel inlet flow rate
$Q_{in,air}$	33 nlpm	Air inlet flow rate
$x_{H_2,in}$	0.115	Hydrogen mole fraction at the fuel inlet
$x_{O_2,in}$	0.21	Oxygen mole fraction at the air inlet

3.2.1 Model validation

Figure 10 shows the comparisons of the polarization curves and temperatures at the center of the stack from the experimental data and simulations for the 15-cell stack under the electrolysis operation mode. The match between the experimental and simulation IVs is not as good as the one for the SOFC operation mode, shown in Figure 2, since the TPBs correcting factor optimized for the SOFC operation mode is used here as well. Still, a decent match is seen between the IVs from the experiment and the simulation.

Under the electrolysis operation mode, the overall reaction is endothermic, and so its heat sink counteracts the ohmic heat sources from the overpotentials. The heat sink from the overall reaction is dominant at lower load currents, while the ohmic heat sources are dominant for higher load currents. Therefore, the temperature is reduced with the load current for lower load currents, reaches a thermoneutral operating point at medium load currents, and increases with the load current afterward. Again, like the SOFC operation mode, the model predicts the temperature evolution with the load current well, but there are deviations between the experimental and simulation values. However, there are other reasons such as: 1) the furnace temperature is fixed in the simulations since during stack testing the furnace setting pointing was fixed. However, the real furnace temperature may be lowered to maintain the same as setting point in the experiments under the SOFC operation mode due to the exothermal reaction, and 2) a steady state is considered for each operating load current in simulations while the experimental data do not show a stationary operation (especially at the beginning for lower load currents) due to a high load current rate of 1 A/min used in the experiments, which could lead to delay in temperature change due to the low heat transfer rate compared with the current rate .

Potential other reasons are the same as stated in.

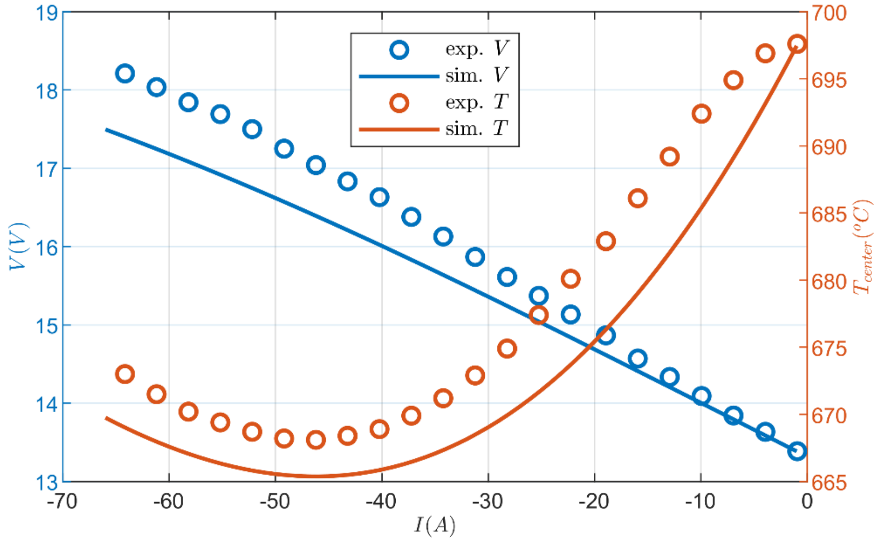

Figure 10: Comparisons of the polarization curves and temperatures at the center of the stack from the experimental data and simulations for the 15-cell stack under the electrolysis operation mode

3.2.2 Species distribution

Figure 11 shows the distributions of the hydrogen and oxygen mole fractions for the 15-cell stack at the load current density of -60.5 A. Hydrogen and oxygen mole fractions increase from the inlet, at the front of the stack, to the outlet, at the back of the stack, due to their generation over the active area under the SOEC operation mode. Again, it should be noted that thanks to the novel header design in this stack, the hydrogen and oxygen mole fractions are almost uniform across the stack in the x-direction. However, the side air channel between the active area and the side part, which is used for better heat transfer inside the stack, leads to an air flow skipping the active area and flowing directly from the inlet to the outlet.

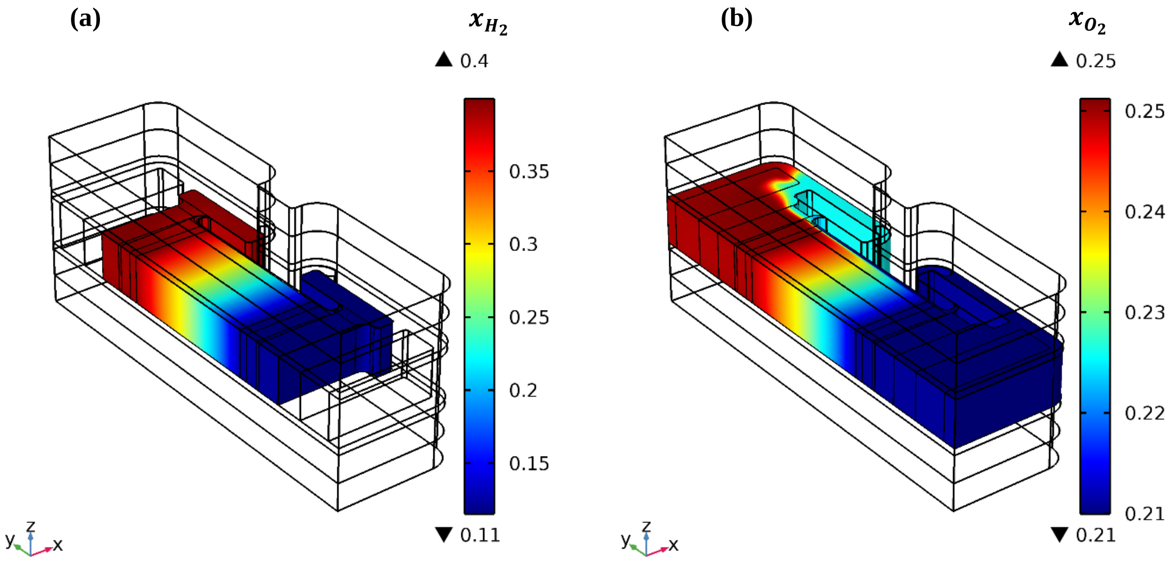

Figure 11: Distributions of (a) hydrogen mole fraction and (b) oxygen mole fraction for the 15-cell stack at the load current of -60.5 A

3.2.3 Temperature distribution

Figure 12 shows the temperature distribution over the whole stack for the 15-cell stack at the load current of -60.5 A. As mentioned in Section 3.2.1, the heat sink from the overall reaction counteracts the heat sources from the overpotentials under the SOEC operation mode. At low current densities, the heat sink from the overall reaction is dominant over the heat sources from the overpotentials, so the temperature decreases from the inlet to the outlet for current densities lower than the thermoneutral operating point. Figure 10 shows that the load current of -60.5 A is lower than the thermoneutral operating point, so it has an overall endothermic trend, as shown in Figure 12. It should be mentioned that the thermal boundary conditions over the outer boundaries of the stack are defined as radiation with ambient at the furnace temperature and convection with air at the furnace temperature. This is why the temperature is not uniform over the outer boundaries of the stacks and is a bit higher for the current collectors' boundaries.

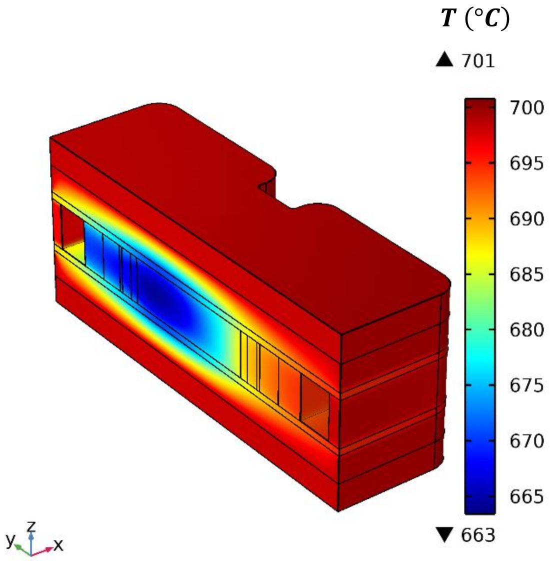

Figure 12: Temperature distribution for the 15-cell stack at the load current of -60.5 A

3.2.4 ASR distribution

Figure 13 shows the ASR distribution for the 15-cell stack at the load current of -60.5 A. The ASR is lower/higher at the inlet/outlet of the active area due to higher/lower temperatures at the inlet and outlet, respectively, as shown in Figure 12.

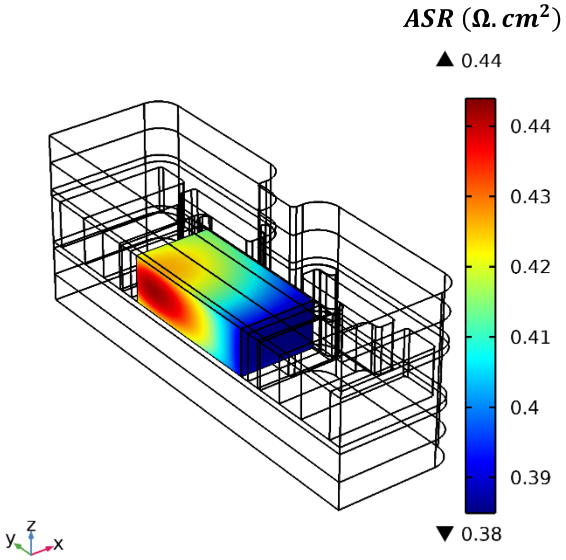

Figure 13: ASR distribution for the 15-cell stack at the load current of -60.5 A

3.2.5 Current density distribution

Figure 14 shows the current density distribution for the 15-cell stack at the load current of -60.5 A. The common trend of maximum/minimum current densities magnitudes at the inlet/outlet of the active area is seen. The reason is the maximum amount of the fuel (/steam) and minimum ASR at the inlet of the active area. It should be noted that for the operating conditions considered here, the ASR magnitude is not high enough to push the current density away from the inlet like the case observed for the 39-cell under SOFC operation mode, shown in Figure 7.

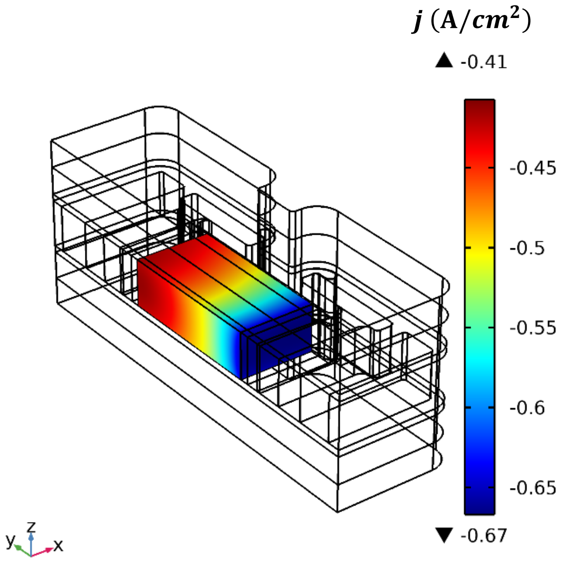

Figure 14: Current density distribution for the 15-cell stack at the load current of -60.5 A

3.2.6 Pressure distribution

Figure 15 shows the distributions of the air and fuel pressures for the 15-cell stack at the load current of -60.5 A. The flow boundary conditions are defined as the flow rate at the inlet, values given in Table 4, and the outlet pressure is set to atmospheric pressure. It needs to be mentioned that the colorbars show the gauge pressure. Therefore, the maximum pressures at the inlets show the pressure drops along the stack for each flow field. Again, thanks to the novel header design in this stack, the pressures are almost uniform across the stack in the x-direction.

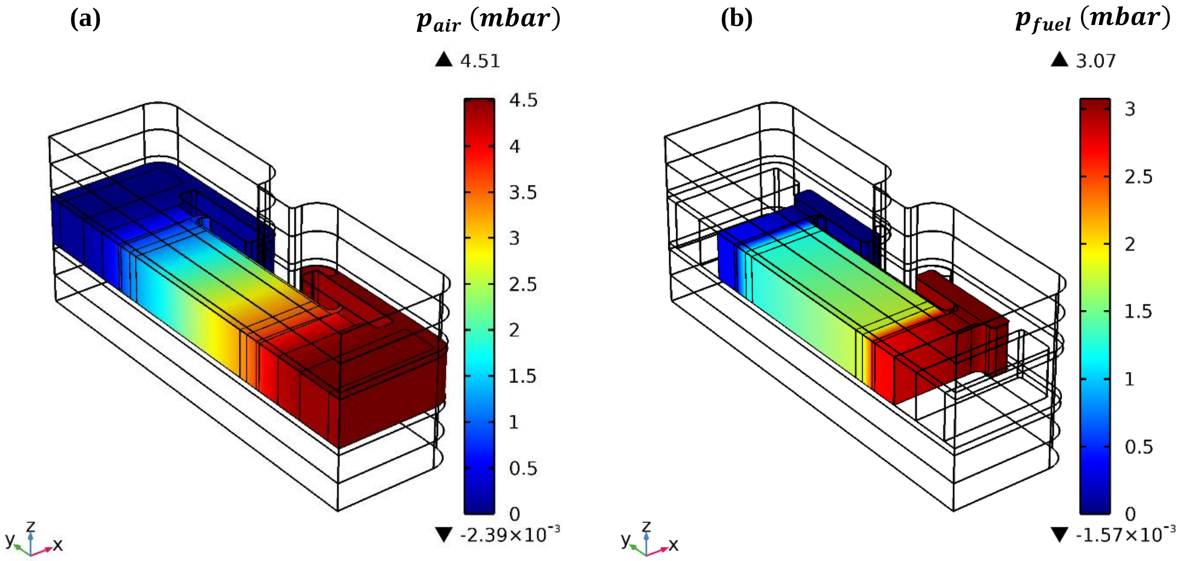

Figure 15: Distributions of (a) air pressure and (b) fuel pressure for the 15-cell stack at the load current of -60.5 A. The colorbars show the gauge pressure values.

4 3D stack-scale Multiphysics mechanical modeling

In this section, a solid mechanics model is added to the multi-scale model presented in Section 3. A detailed description of the solid mechanics' governing equations and their parameters calculations for the homogenized stack model can be found in our previous works [2,4]. The solid mechanics model uses the temperature distribution over the stack to evaluate the thermal stresses in addition to the stresses induced by an external load over the stack. It should be noted that the stresses calculated by the model are the effective (/average) ones over the whole homogenized domain. For detailed stress distributions over the cell layers, detailed sub-models with external loading from the homogenized stresses are needed [4].

4.1 Fuel cell operation mode

This section presents the modeling results for the 15- and 39-cell stacks under the fuel cell operation mode. The operating conditions are listed in Table 3.

4.1.1 15-cell stack

Figure 16 shows the distribution of the principal stresses over the whole stack and the active area for the 15-cell stack at the load current density of 0.25 A/cm^2. Where Sigma 1 is the maximum principal stress, sigma 2 is the intermediate principal stress, and sigma 3 is the least principal stress. For the whole stack, very high stresses values are seen at the interfaces between different layers, which is due to numerical difficulties induced by the properties changes between different layers. This is why the stress distributions for the active area, which is of the most interest to us, are also shown. One can see that the higher temperature at the outlet of the active area due to the SOFC operation mode, as discussed in Section 3.1.3, leads to compressive stresses over the stack components.

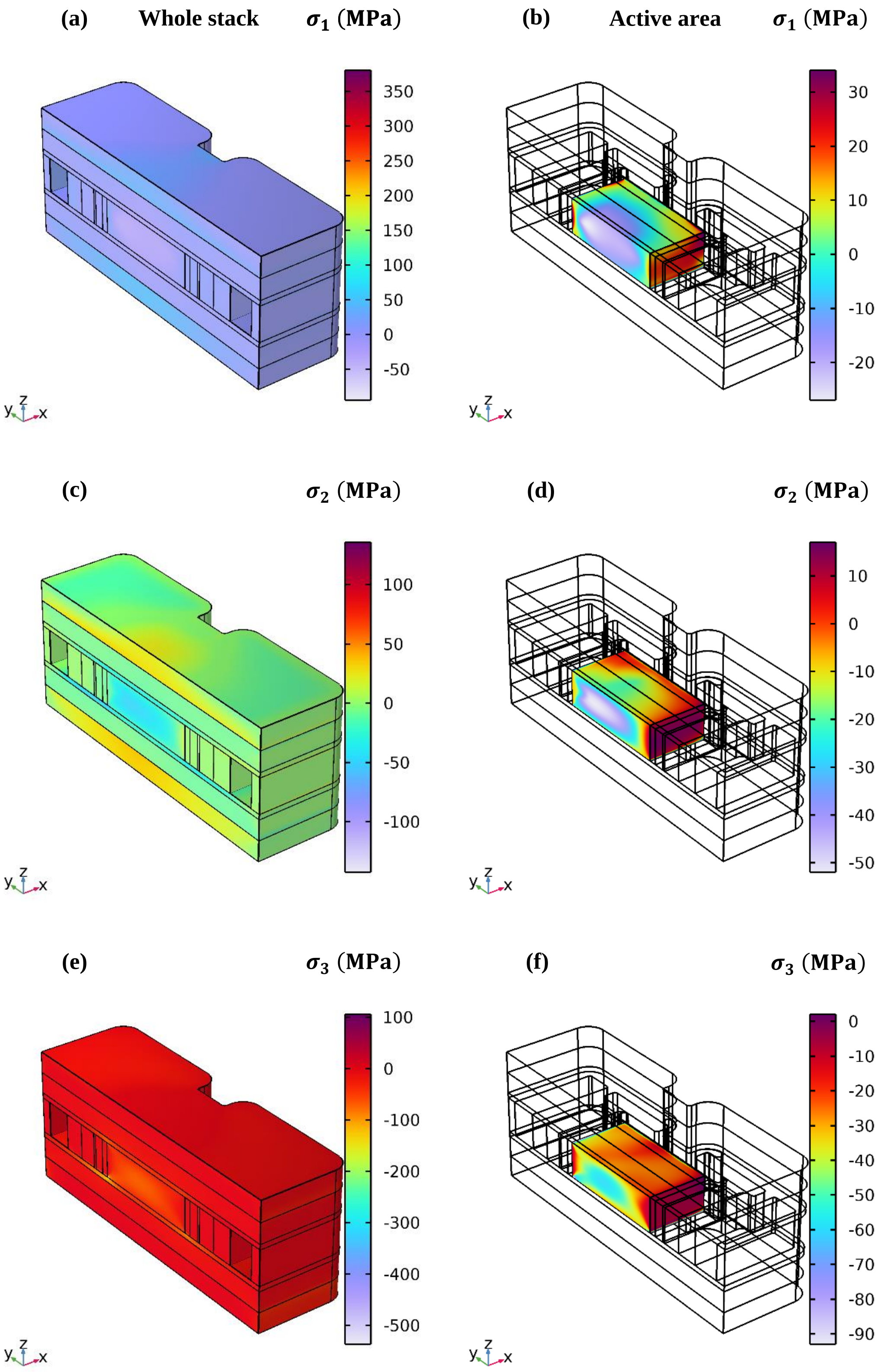

Figure 16: Distributions of the principal stresses over the whole stack (a, c, and e) and the active area (b, d, and f) for the 15-cell stack at the load current density of 0.25 A/cm²

Figure 17a-f shows the variations of the principal stresses maximums and minimums over the active area *versus* the load current density for the 15-cell stack. The magnitudes of the maximum and minimum stresses increase with the load current density, which is due to the higher temperature gradients over the active area for higher load current densities, as shown in Figure 17g.

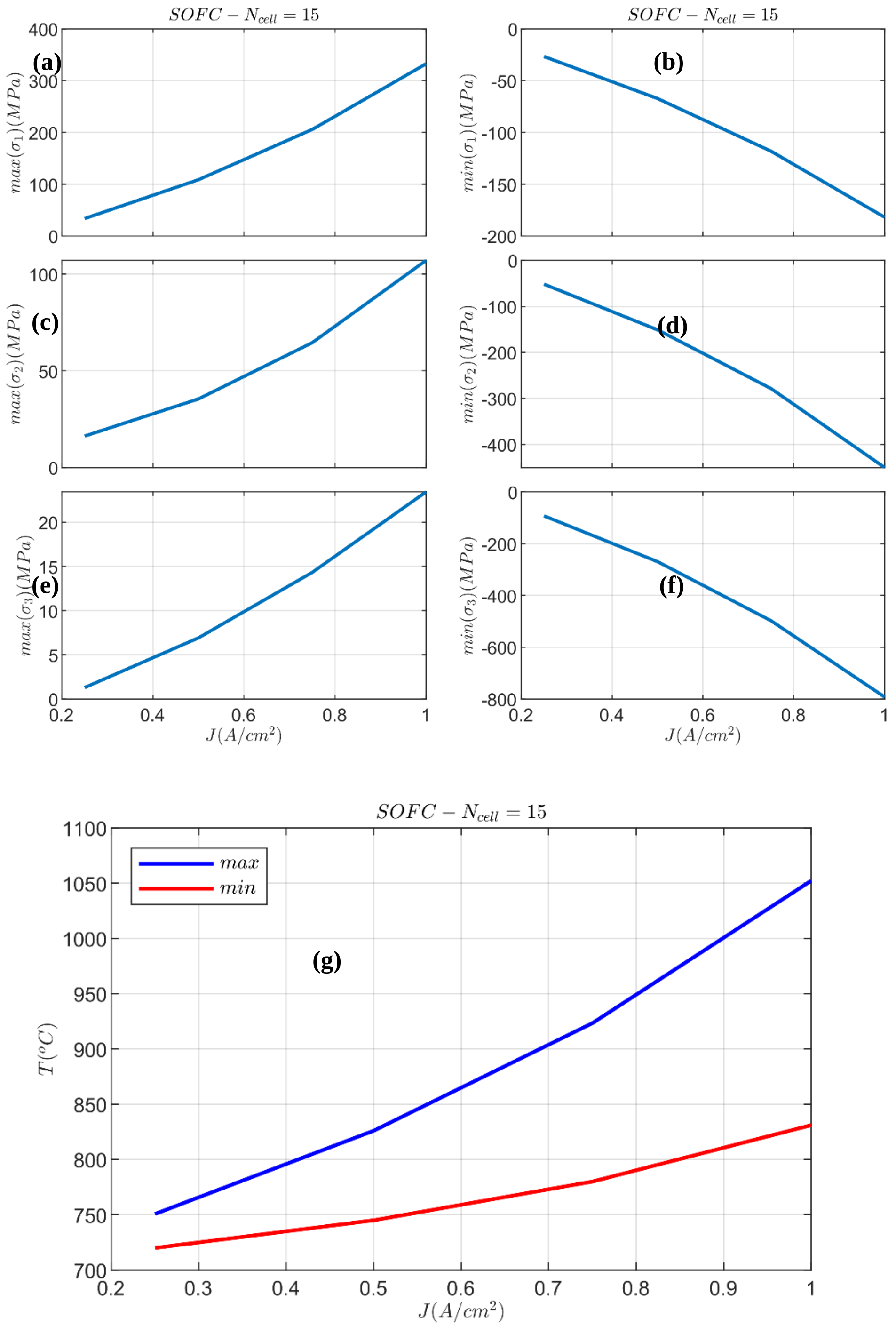

Figure 17: Variations of the principal stresses maximum (a, c, and e) and minimum (b, d, and f) and the maximum and minimum of the temperature (g) over the active area versus the load current density for the 15-cell stack

4.1.2 39-cell stack

Figure 18 shows the distributions of the principal stresses over the whole stack and the active area for the 39-cell stack at the load current density of 0.25 A/cm^2. Again, very high stresses values are seen at the interfaces between different layers for the whole stack, which is due to numerical difficulties induced by the properties changes between different layers. This is why the stress distributions for the active area, which is of the most interest to us, are also shown. One can see that the higher temperature at the outlet of the active area due to the SOFC operation mode, as discussed in Section 3.1.3, leads to compressive stresses over the stack components.

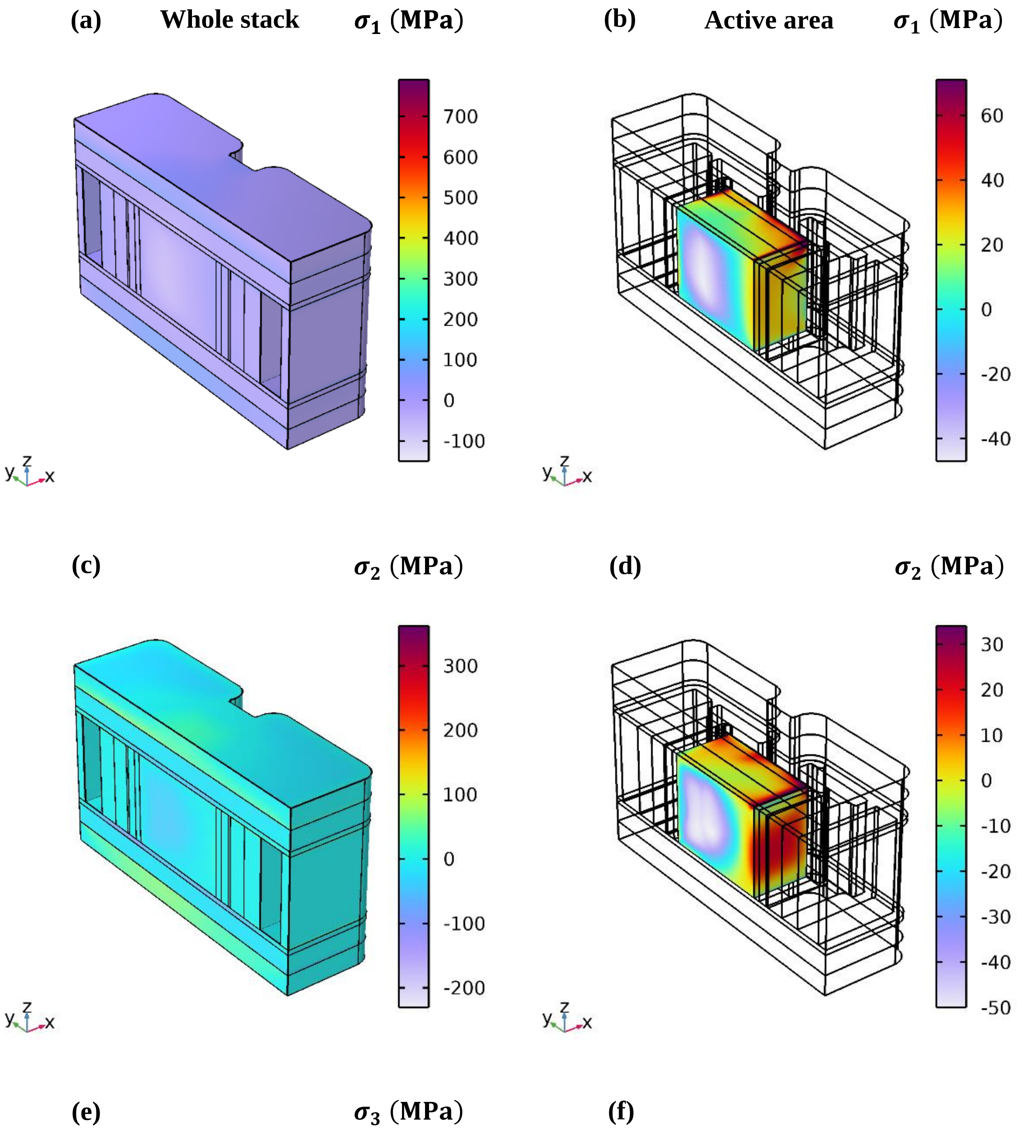

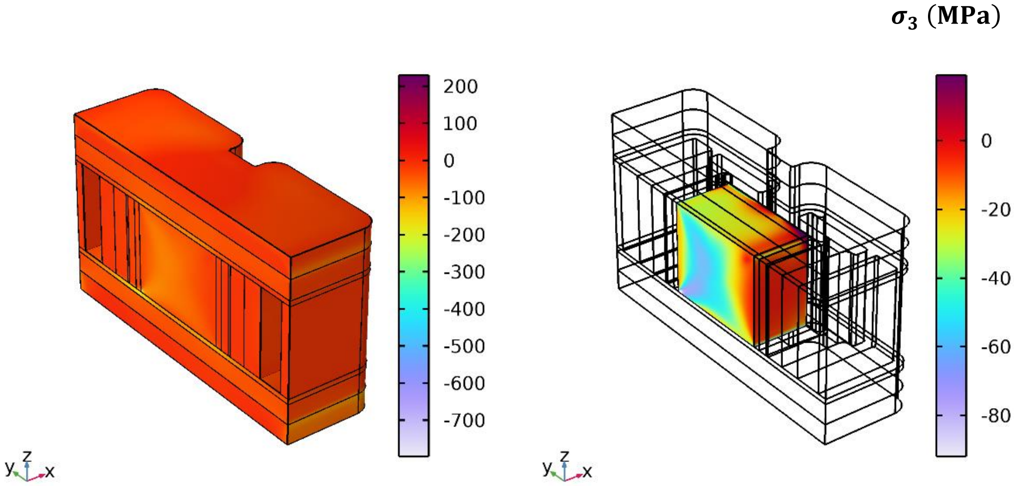

Figure 18: Distributions of the principal stresses over the whole stack (a, c, and e) and the active area (b, d, and f) for the 39-cell stack at the load current density of 0.25 A/cm²

Figure 19a-f shows the variations of the principal stresses maximums and minimums over the active area *versus* the load current density for the 39-cell stack. The magnitudes of the maximum and minimum stresses increase with the load current density, which is due to the higher temperature gradients over the active area for higher load current densities, as shown in Figure 19g. The unexpected drop in the third principal stress maximum at the load current density of 0.5 A/cm^2, shown in Figure 19e, could be due to the propagation of the singularity at the interfaces to the active area, as shown in Figure 18f.

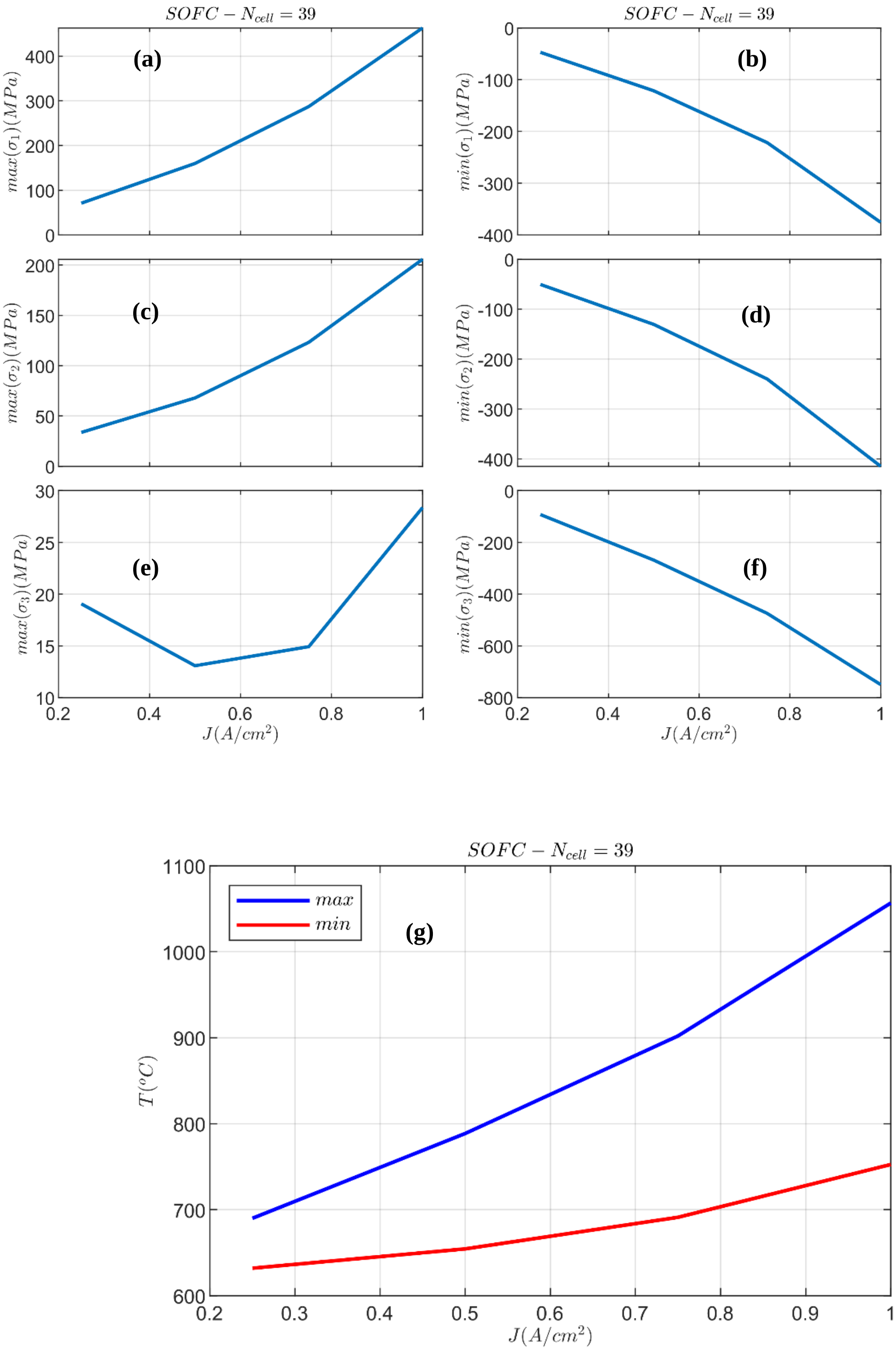

Figure 19: Variations of the principal stresses maximum (a, c, and e) and minimum (b, d, and f) and the maximum and minimum of the temperature (g) over the active area versus the load current density for the 39-cell stack

4.2 Electrolysis operation mode

This section presents the modeling results for the 15- and 39-cell stacks under the electrolysis operation mode. The operating conditions are listed in Table 5.

Table 5: Operating conditions for the 15- and 39-cell stacks under the SOEC operation mode

Parameter	Value, 15-cell stack	Value, 39-cell stack	Description
p_{op}	1 atm	1 atm	Operating pressure
T_{in}	699 °C	699 °C	Inflow temperature
$T_{furnace}$	699 °C	699 °C	Furnace temperature
$Q_{in,fuel}$	11.72 nlpm	40 nlpm	Fuel inlet flow rate
$Q_{in,air}$	33 nlpm	86 nlpm	Air inlet flow rate
$x_{H_2,in}$	0.115	0.115	Hydrogen mole fraction at the fuel inlet
$x_{O_2,in}$	0.21	0.21	Oxygen mole fraction at the air inlet

4.2.1 15-cell stack

Figure 20 shows the distributions of the principal stresses over the whole stack and the active area for the 15-cell stack at the load current density of -0.25 A/cm^2. For the whole stack, very high stresses values are seen at the interfaces between different layers, which is due to numerical difficulties induced by the properties changes between different layers. This is why the stress distributions for the active area, which is of the most interest to us, are also shown. One can see that the lower temperature at the outlet of the active area due to the SOEC operation mode, as discussed in Section 3.2.3, leads to tensile stresses over the stack components.

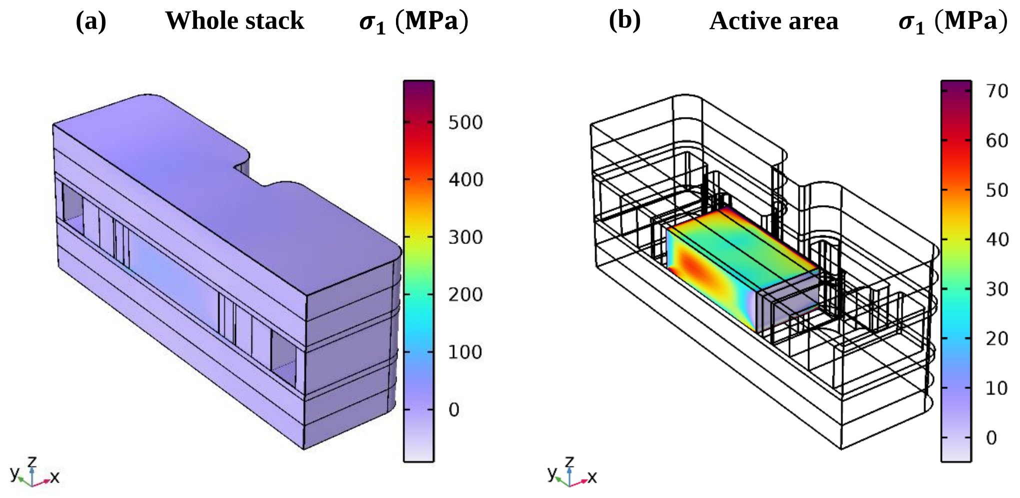
(a) **Whole stack** **σ_1 (MPa)**

(b) **Active area** **σ_1 (MPa)**

(c)

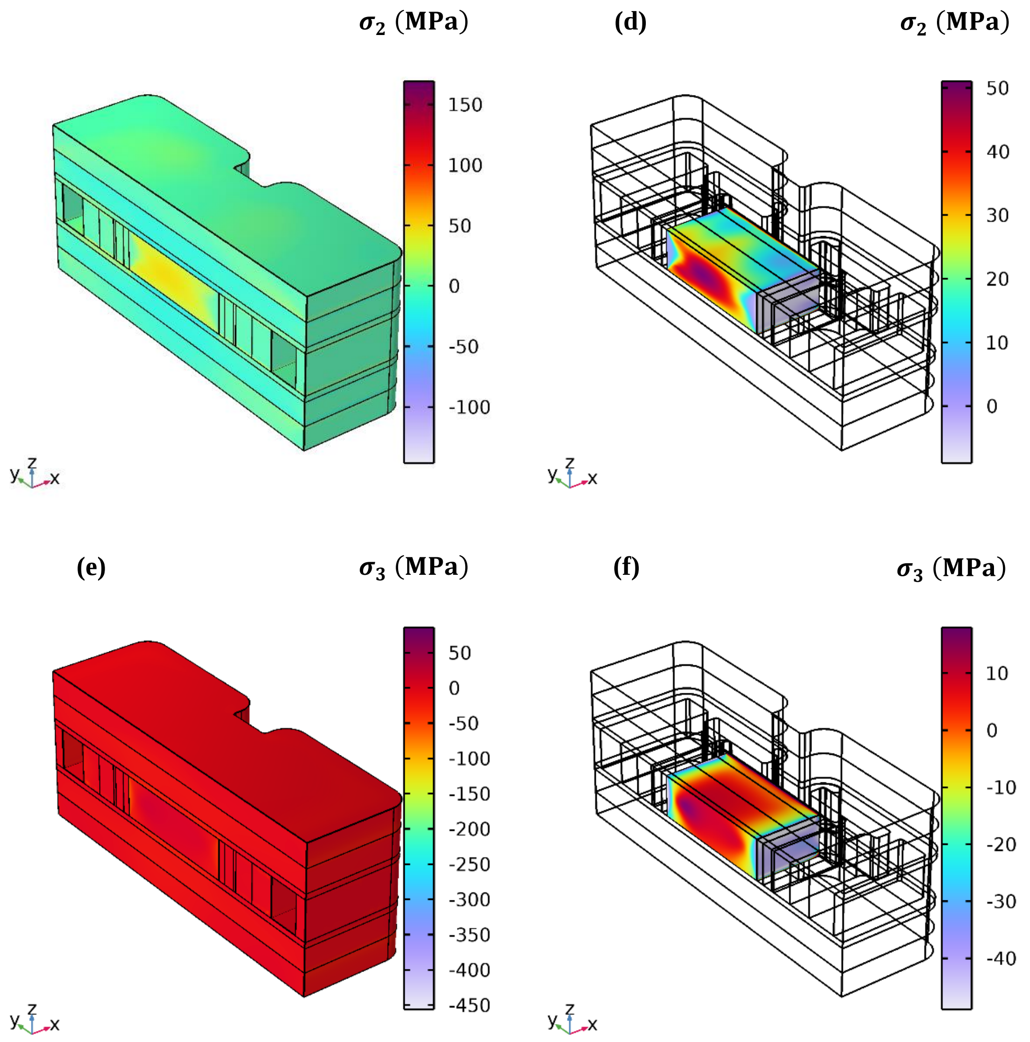

Figure 20: Distributions of the principal stresses over the whole stack (a, c, and e) and the active area (b, d, and f) for the 15-cell stack at the load current density of -0.25 A/cm^2

Figure 21a-f shows the variations of the principal stresses maximums and minimums over the active area *versus* the load current density for the 15-cell stack. The magnitudes of the maximum and minimum stresses increase with the load current density magnitude from -0.25 to -0.5 A/cm^2, which is due to the higher temperature gradient over the active area as shown in Figure 21g, and they reduce afterward, which is due to the lower temperature gradients over the active area for higher load current densities, as shown in Figure 21g. Moreover, Figure 21g indicates that the stack gets into the exothermic regime for the load current density of -1 A/cm^2. This change in the thermal mode of the stack could be the reason for the trend change of the minimums of the first and second principal stresses between the load current densities of -0.75 and -1 A/cm^2, as shown in Figure 21b and Figure 21d.

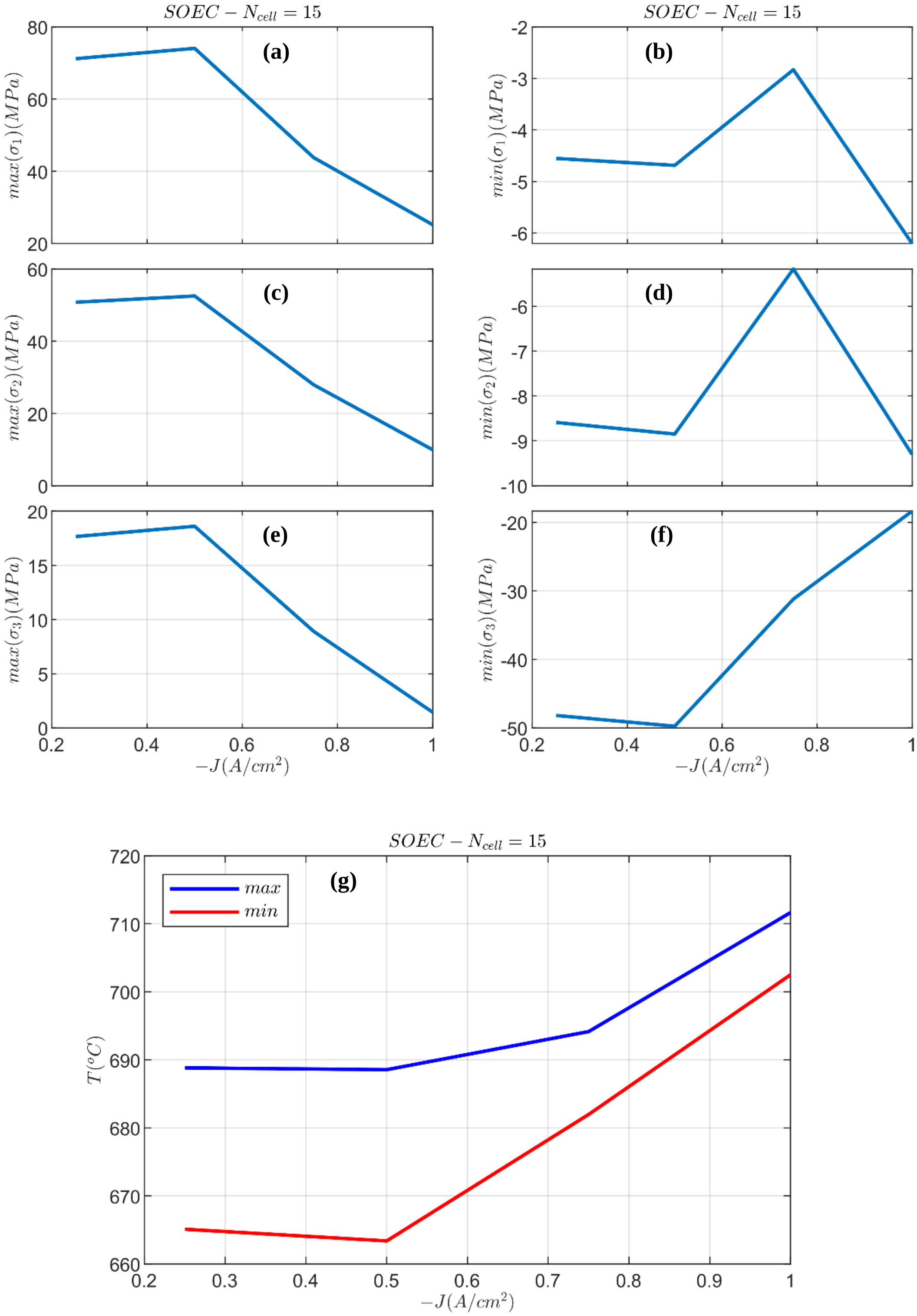

Figure 21: Variations of the principal stresses maximum (a, c, and e) and minimum (b, d, and f) and the maximum and minimum of the temperature (g) over the active area versus the load current density for the 15-cell stack

4.2.2 39-cell stack

Figure 22 shows the distribution of the principal stresses over the whole stack and the active area for the 39-cell stack at the load current density of -0.25 A/cm^2. Again, very high stress values are seen at the interfaces between different layers for the whole stack, which is due to numerical difficulties induced by the properties changes between different layers. This is why the stress distributions for the active area, which is of the most interest to us, are also shown. One can see that the lower temperature at the outlet of the active area due to the SOEC operation mode, as discussed in Section 3.2.3, leads to tensile stresses over the stack components.

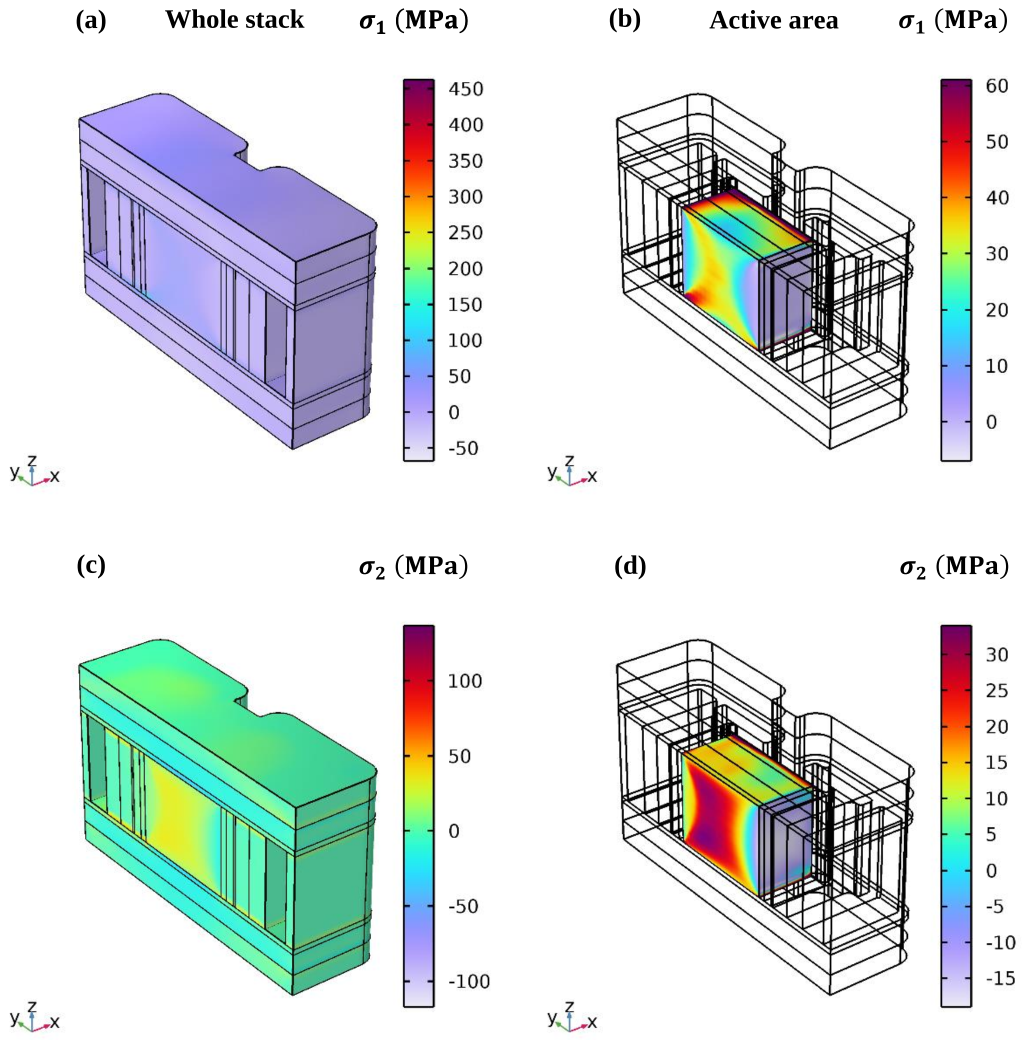

(e) σ_3 (MPa) **(f)**

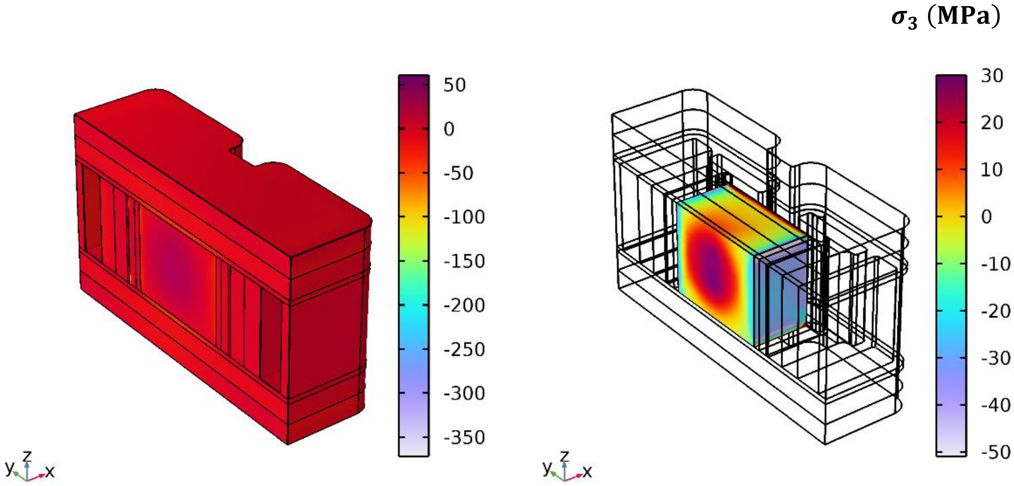

Figure 22: Distributions of the principal stresses over the whole stack (a, c, and e) and the active area (b, d, and f) for the 39-cell stack at the load current density of -0.25 A/cm^2

Figure 23a-f shows the variations of the principal stresses maximums and minimums over the active area *versus* the load current density for the 39-cell stack. The magnitudes of the maximum and minimum stresses increase with the load current density magnitude from -0.25 to -0.5 A/cm^2, which is due to the higher temperature gradient over the active area as shown in Figure 23g, and they reduce afterward, which is due to the lower temperature gradients over the active area for higher load current densities, as shown in Figure 23g. Moreover, Figure 23g indicates that the stack gets into the exothermic regime for the load current density of -1 A/cm^2. Here, the temperature gradient under the exothermic regime is not as high as the one for the 15-cell stack, so changes in all the maximums and minimums of the principal stresses with the load current density are monotonous for this 39-cell stack.

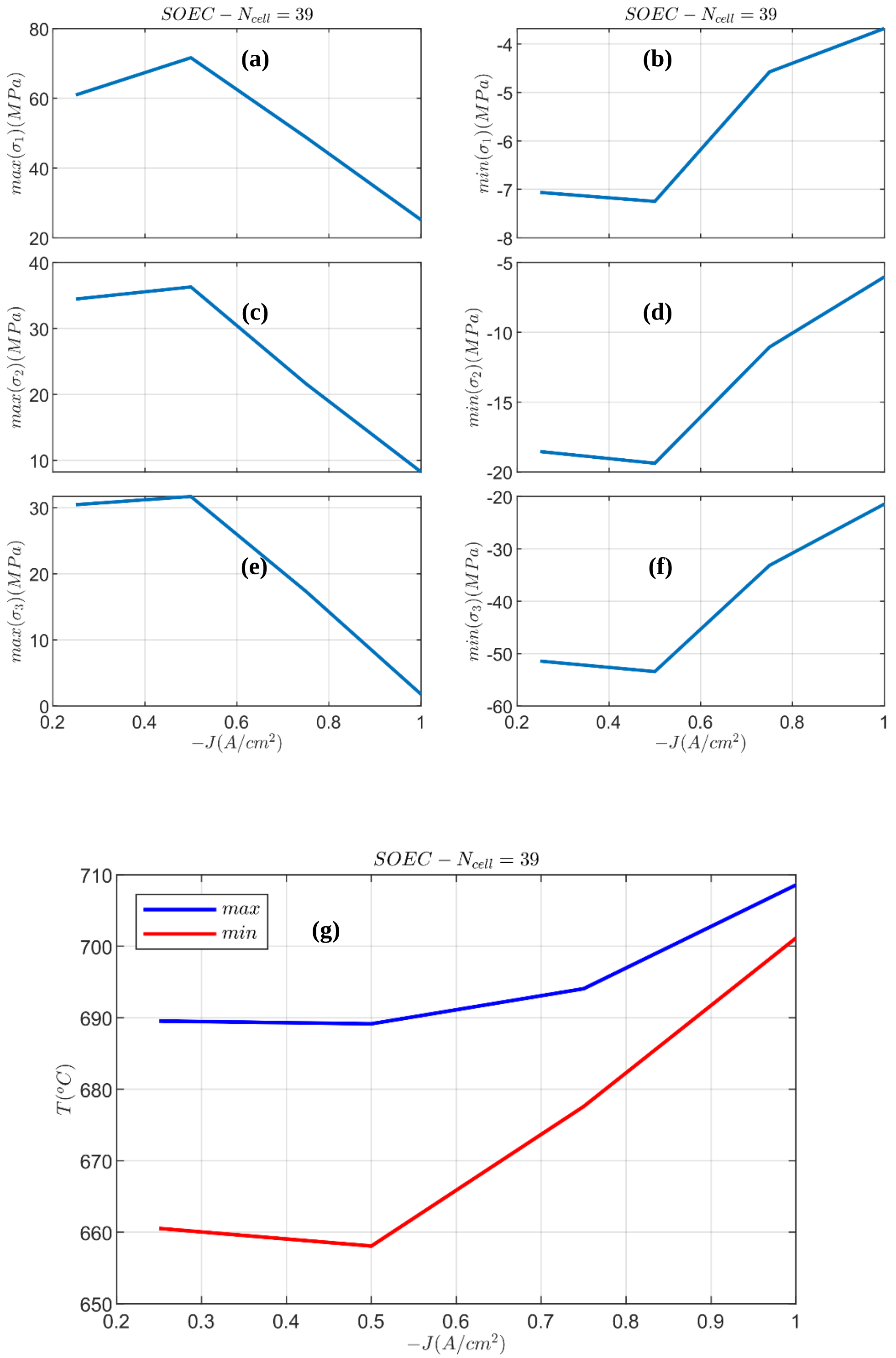

Figure 23: Variations of the principal stresses maximum (a, c, and e) and minimum (b, d, and f) and the maximum and minimum of the temperature (g) over the active area versus the load current density for the 39-cell stack

5 0D and ½D cell models

Table 6 lists the governing equations used for the cell model. The cell voltage is defined as the reversible cell voltage minus the sum of overpotentials, Eq. (15). Butler-Volmer (BV) equation, Eq. (18), is used to determine the activation overpotentials. Exchange current densities are defined by Arrhenius-type equations multiplied by the ratios of the species partial pressures and reference pressure, Eqs. (19) and (20). The concentration overpotentials are determined based on the mole fractions of the species at the electrodes/interconnect and electrode/electrolyte interfaces, Eqs. (21) and (22). The ohmic overpotential is assumed to follow an Arrhenius-type equation, Eq. (23).

Table 6: Cell model equations

Description	Governing equation	Eq. #
Cell voltage [2]	$V_{cell} = E_{eq} - (\eta_{act,an} + \eta_{act,ca} + \eta_{conc,an} + \eta_{conc,ca} + \eta_{ohm})$	(15)
Open-circuit voltage (OCV) [2]	$E_{eq} = \frac{\Delta G}{nF} + \frac{RT}{nF} ln(\frac{p_{H_2}\, p_{O_2}^{0.5}}{p_{H_2O}\, p_{ref}^{0.5}})$	(16)
Gibbs free energy [14]	$\Delta G = -0.0031T^2 - 49119T + 244778$	(17)
Butler-Volmer (BV) [12]	$J = J_{0,an/ca} \left[exp(-\alpha_{an/ca} \frac{nF\eta_{act,an/ca}}{RT}) - exp(-(1 - \alpha_{an/ca}) \frac{nF\eta_{act,an/ca}}{RT})\right]$	(18)
Anode exchange current density [12]	$J_{0,an} = \gamma_{an} \left(\frac{p_{O_2}}{p_{ref}}\right)^m exp(\frac{-E_{act,an}}{RT})$	(19)
Cathode exchange current density [12]	$J_{0,ca} = \gamma_{ca} \left(\frac{p_{H_2}}{p_{ref}}\right)^a \left(\frac{p_{H_2O}}{p_{ref}}\right)^b exp(\frac{-E_{act,ca}}{RT})$	(20)
Anode concentration overpotential [15]	$\eta_{conc,an} = \frac{RT}{2F} ln((\frac{x_{O_2}^I}{x_{O_2}^0})^{0.5})$	(21)
Cathode concentration overpotential [15]	$\eta_{conc,ca} = \frac{RT}{2F} ln(\frac{x_{H_2}^I\, x_{H_2O}^0}{x_{H_2}^0\, x_{H_2O}^I})$	(22)
Ohmic overpotential [12]	$\eta_{ohm} = J \frac{T}{B_{ohm}} exp(\frac{E_{act,ohm}}{RT})$	(23)
Dusty-gas model (DGM) fluxes [16]	$\frac{N_1}{D_{1K}^{eff}} + \frac{x_2N_1 - x_1N_2}{D_{12}^{eff}} = -\frac{1}{RT}(p\nabla x_1 + x_1\nabla p + x_1\nabla p)\frac{kp}{D_{1K}^{eff}\, \mu}$	(24)
	$\frac{N_2}{D_{1K}^{eff}} + \frac{x_1N_2 - x_2N_1}{D_{12}^{eff}} = -\frac{1}{RT}(p\nabla x_2 + x_2\nabla p + x_2\nabla p)\frac{kp}{D_{2K}^{eff}\, \mu}$	(25)
Binary diffusion coefficient [17]	$D_{ij} = \frac{0.00143\, T^{1.75}}{PM_{ij}^{0.5}({V_i}^{1/3} + {V_j}^{1/3})^2}; M_{ij} = \frac{2}{M_i^{-1} + M_j^{-1}}$	(26)
Knudsen diffusion coefficient [14]	$D_{ik} = \frac{d_p}{3}\sqrt{\frac{8RT}{\pi M_i}}$	(27)
Effective diffusion coefficient	$D_{ij}^{eff,an/ca} = k_{D,eff}^{an/ca} D_{ij}^{an/ca}$	(28)
Inlet molar flow rate	$\dot{n}_{in} = Q_{in} \frac{p}{RT}$	(29)
Species molar flow rate at the inlet	$\dot{n}_{in,i/j} = x_{in,i/j}\, \dot{n}_{in}$	(30)
Species molar flow rate at the outlet	$\dot{n}_{out,i/j} = \dot{n}_{in,i/j} + \dot{n}_{react,i/j}$	(31)
Species mole fraction at the outlet	$x_{out,i/j} = \frac{\dot{n}_{out,i/j}}{\dot{n}_{out,i} + \dot{n}_{out,j}}$	(32)

In equations (21) and (22), superscripts I and 0 represent the locations of the species at the electrode/electrolyte and the electrode/interconnect interface, respectively. Mole fractions of the species at the electrode/interconnect interface are set to their values at the inlet and outlet. Still, species mole fractions at the electrode/electrolyte interface need to be determined. The dusty-gas model (DGM) is used to model species transport between the electrode surface and electrode/electrolyte interface. A modified version of the DGM with independent molar fluxes for a binary gas is used, Eqs. (24) and (25). By equating these fluxes to the ones for the species consumed/generated at the reaction sites, which is given by Faraday's Law of reactions as j/nF, mole fractions of the species at the electrode-electrolyte interfaces are calculated. These values are substituted in equations (21) and (22) to calculate the concentration overpotentials.

The common Bruggemen correction used to modify the diffusion coefficients in porous media, e.g. [14], is not considered. Instead, a single coefficient is used to modify the diffusion coefficients in each side of the cell to reduce the number of unknowns from 4 (porosities and tortuosities for both sides) to 2, Eq. (28).

For the 0D model, the species concentrations are fixed and set to their values at the inlets, as shown in Figure 24. However, species distributions over the active area affect the OCV and activation and concentration overpotentials. To add the effect of the species variations over the active area, the OCV and activation and concentration overpotentials are calculated at the inlet and outlet, and their averages are used for the cell voltage calculation, Eq. (15). The species composition is known at the inlet but not at the outlet, which can be determined through species conservation based on their inlet conditions and reactions, as shown in Eqs. (29)-(32). We call this cell model a ½D model, shown in Figure 24, with the species concentrations known at the inlet and outlet.

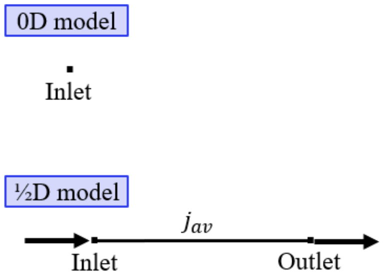

Figure 24: 0D and ½D cell models

The ½D cell model is used to evaluate its polarization characteristic (IV). MATLAB is used to fit the model to the measured polarization curves and identify a set of material parameters for the cell model. Load current densities are considered as knowns/inputs to solve for their corresponding cell voltages. Calculating the ohmic and concentration overpotentials is straightforward as they are explicit functions of the current density. Since the activation overpotentials are implicit functions of the current density, Eq. (18), the "fsolve" function is used to solve for them through solving a system of nonlinear equations with two equations and two unknowns.

5.1 Optimization

The governing equations presented in the previous section have 13 free parameters, given in Table 7, which can be adjusted by fitting the model polarization curves to the experimental ones. The genetic algorithm with a population size of 10^4 is used to find the optimum values of the parameters that minimize the errors between the cell voltages from the model and the experimental data:

$$f_{ob} = \sqrt{\sum_{i=1}^{n_{oc}} \sum_{k=1}^{n_j} \left(V_{cell,sim} - V_{cell,exp}\right)^2} \tag{33}$$

Here, f_{ob} is the objective function, n_{oc} and n_j are numbers of operating conditions and load current densities, respectively, and abbreviations exp and sim denote the experimental and simulation data, respectively. Operating conditions are given in Figure 25. 50 load current densities between the maximum and minimum current densities given in Figure 25 are used. It should be noted that the experimental data are interpolated over these current densities so that we have the same operating points as the ones used in the simulation for calculating the error between the experimental and simulation data, Eq. (33).

Table 7: Optimum values of the fitting parameters from GA

Parameter	Value	Description
$\gamma_{0,an}$	1948768.2217 A m^{-2} K^{-1}	Constant of the prefactor used for the anode exchange current density
$\gamma_{0,ca}$	783710175.4735 A m^{-2} K^{-1}	Constant of the prefactor used for the cathode exchange current density
$E_{act,an}$	106538.3827 J mol^{-1}	Activation energy used for the anode exchange current density
$E_{act,ca}$	51226.2659 J mol^{-1}	Activation energy used for the cathode exchange current density
α_{an}	0.56011	Charge transfer coefficient of the anode reaction
α_{ca}	0.672	Charge transfer coefficient of the cathode reaction
m	0.19623	Power of the oxygen partial pressure used for the anode exchange current density
a	-0.088749	Power of the hydrogen partial pressure used for the cathode exchange current density
b	0.38112	Power of the steam partial pressure used for the cathode exchange current density
$k_{D,eff}^{an}$	0.020009	Correction factor for the diffusion coefficients of the species in the anode porous media
$k_{D,eff}^{ca}$	0.020009	Correction factor for the diffusion coefficients of the species in the cathode porous media
B_{ohm}	7294098713342.129 S K m^{-2} 58246647010731.87 S K m^{-2}	Material-specific constant used for the ohmic overpotential
$E_{act,ohm}$	92381.6634 J mol^{-1} 105788.1144 J mol^{-1}	Activation energy used for the ohmic overpotential

Table 7 lists the optimum values of the fitting parameters evaluated by the genetic algorithm for the [**ELCOGEN**] cells. Figure 25 compares the polarization curves from the experimental data and the ½D cell model for the optimum values of the fitting parameters given in Table 7. A good match is seen between the polarization curves for all operating conditions.

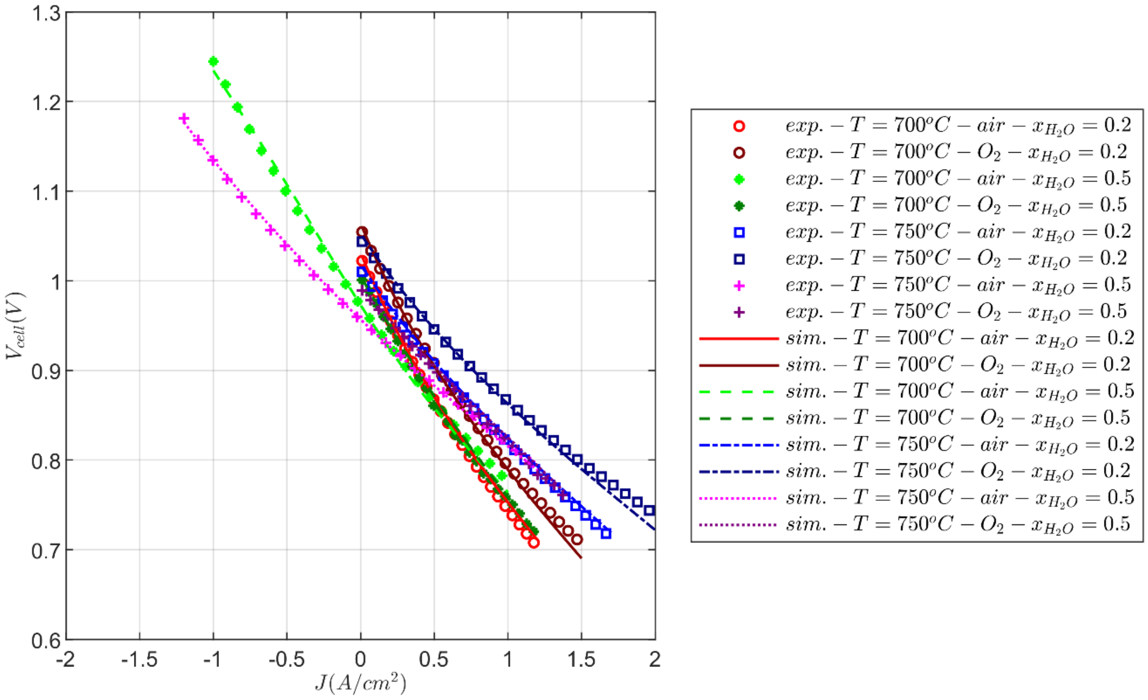

Figure 25: Comparisons of the polarization curves from the experimental data (exp.) and the ½D model (sim.) with the fitted parameters given in Table 7

5.2 Activation overpotentials *vs* current

Figure 26 shows the activation overpotentials from the ½D cell model for the optimum values of the fitting parameters given in Table 7. The common trends of higher activation overpotentials for higher load current densities and lower temperatures are seen.

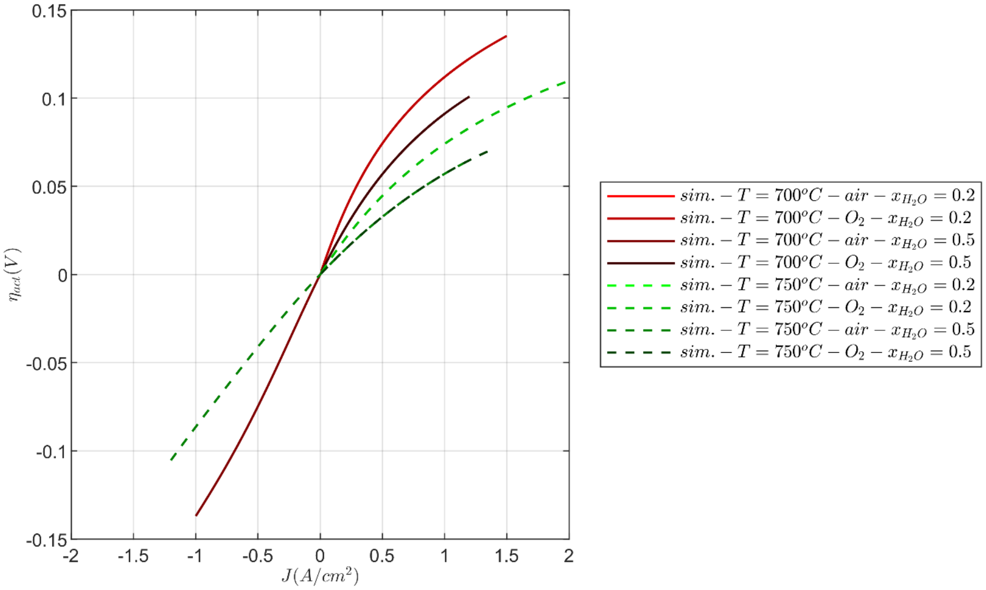

Figure 26: Activation overpotentials from the ½D model (sim.) with the fitted parameters given in Table 7

5.3 Ohmic overpotentials vs current

Figure 27 shows the ohmic overpotentials from the ½D cell model for the optimum values of the fitting parameters given in Table 7. The common trends of higher ohmic overpotentials for higher load current densities and lower temperatures are seen. It is expected that the ohmic overpotential is not a function of the species concentrations. However, Figure 27 shows two different slops for the ohmic overpotentials under each operating temperature. It should be mentioned that these different slops were due to the various Ohmic fitting parameters from different cell test results, where different Ohmic resistance were observed, and this is also the reason for two different ohmic parameter sets given in Table 7.

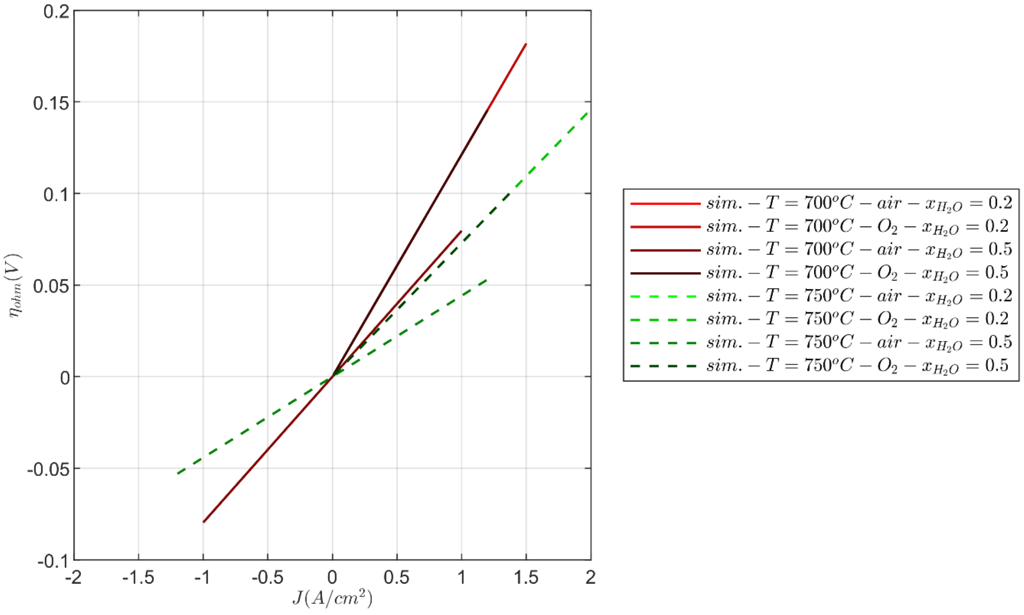

Figure 27: Ohmic overpotentials from the ½D model (sim.) with the fitted parameters given in Table 7

5.4 Concentration overpotentials vs current

Figure 28 shows the concentration overpotentials from the ½D cell model for the optimum values of the fitting parameters given in Table 7. The common trends of higher concentration overpotentials for higher load current densities and lower concentration overpotentials for the 50/50 concentrations of the hydrogen/steam are seen.

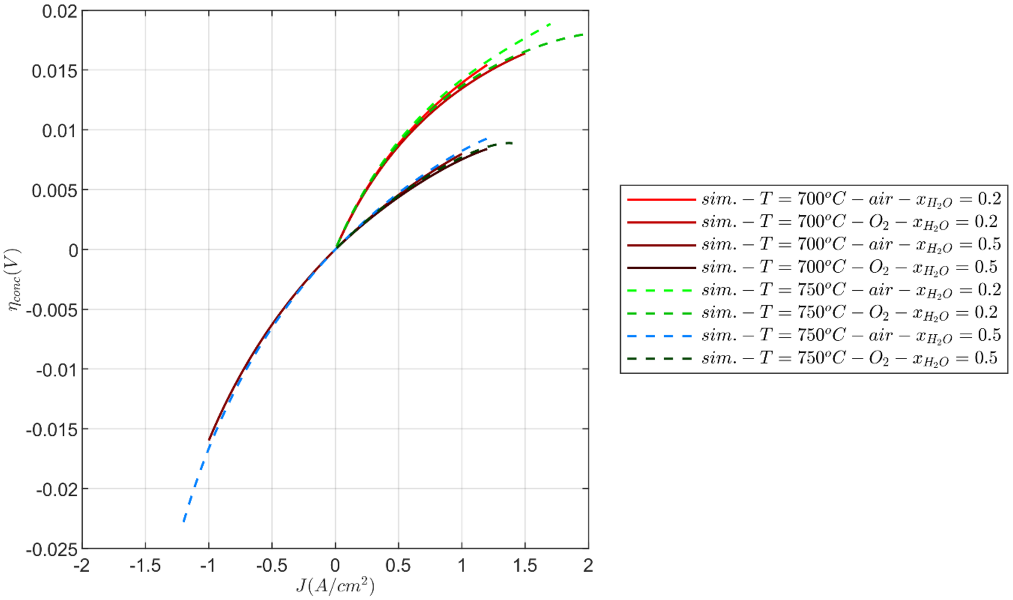

Figure 28: Concentration overpotentials from the ½D model (sim.) with the fitted parameters given in Table 7

6 1D cell model

The 1D cell model divides the cell along the flow to a certain number of elements, as shown in Figure 29. The species conservation is applied to the inlet and outlet of each element, starting from the first element at the inlet and proceeding to the last one at the outlet. Evaluating the species concentrations on the out node of each element is similar to what is done in the ½D model for evaluating the outlet species concentrations based on their inlet conditions and reactions, as given in Eqs. (29)-(32).

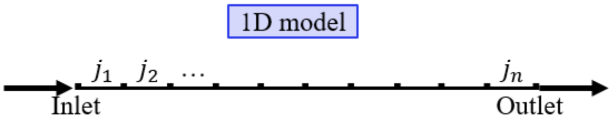

Figure 29: 1D cell model

Figure 30 shows the comparisons of the polarization curves from the experimental data and the 1D cell model for the optimum values of the fitting parameters given in Table 7. A good match is seen between the simulation and experimental polarization curves, which indicates that the parameters from the optimization with the ½D model are reliable. Nonetheless, there are slight deviations between the polarization curves for higher current densities under the SOEC operation mode. Therefore, the fitting parameters from the ½D model are not much accurate for evaluating the cell characteristic under high current densities where the concentration overpotentials are dominant.

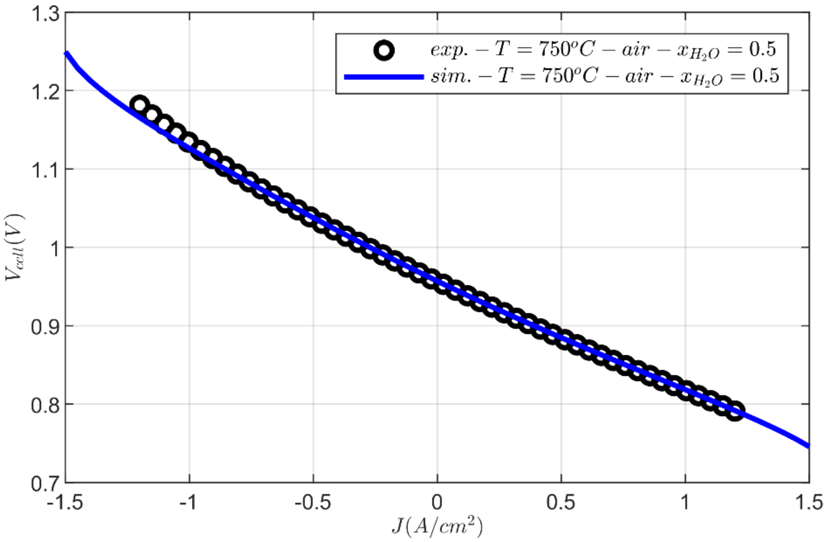

Figure 30: Comparisons of the polarization curves from the experimental data (exp.) and the 1D model (sim.) with the fitted parameters given in Table 7

6.1 Modelling variables distributions

Figure 31 shows the distributions of the current density, OCV, activation and concentration overpotentials, and hydrogen and oxygen mole fractions along the cell (x-axis) from the inlet to the outlet for the operating conditions given in Figure 30 and the fitting parameters given in Table 7. The distributions are given at the load current densities of 0.5, 1, and 1.5 A/cm^2 under both SOFC and SOEC operation modes. In addition to capturing the common trends for the modeling variables distributions, the 1D cell model also predicts their nonlinearities under high current densities.

As expected, the maximum/minimum current densities are located at the inlet/outlet of the cell, and their gradients and nonlinearities get higher for higher load current densities, as shown in Figure 31a. The same trends are seen for the activation overpotential since it is proportional to the current density as indicated by the BV equation (18) and shown in Figure 31c. OCV increases/decreases along the cell under the SOEC/SOFC operation modes, as illustrated in Figure 31b, due to the species conversions along the cell. The concentration overpotential increases exponentially under the high load current density and at the end of the cell with the lowest species concentration, as shown in Figure 31d. Hydrogen and oxygen mole fractions are increasing/decreasing along the cell under the SOEC/SOFC operation modes, as indicated in Figure 31e and Figure 31f.

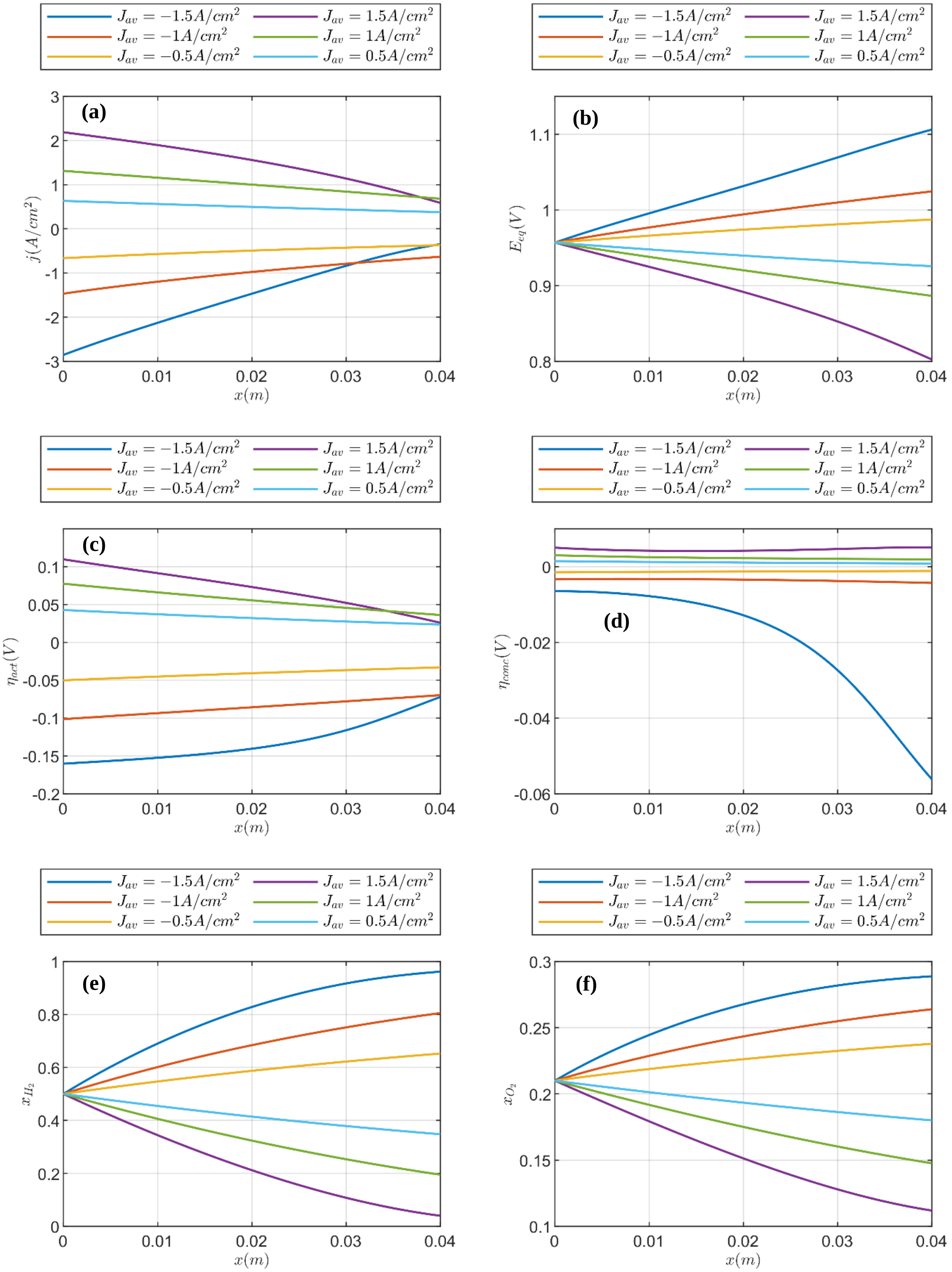

Figure 31: 1D cell model results: distributions of the current density (a), OCV (b), activation overpotential (c), concentration overpotential (d), hydrogen mole fraction (e), and oxygen mole fraction (f) along the flow direction (x-axis) from the inlet to the outlet for the operating conditions given in Figure 30 and the fitted parameters given in Table 7

7 Conclusion

In this work, electrochemical and mechanical model with specific parameter inputs from [**ELCOGEN**] were developed and validated with both cell and stack test results by [**DTU**]. Electrochemical modelling results show that [**ELCOGEN**] stack has very homogenized gas distribution and low pressure drop on both fuel and air side. In SOFC mode, higher temperature can be seen at the outlet of the fuel gas direction resulted in a lower ASR values at the outlet than inlet. However due to the higher H_2 concentration at the fuel inlet, higher current density is expected at the inlet than outlet. While in SOEC mode, lower temperature is expected at the outlet of the fuel stream when operating at below thermoneutral voltage, which resulted in a higher ASR at the outlet than inlet, meanwhile the high steam concentration at the inlet caused higher current at the inlet than outlet. Mechanical model reveals that in SOFC operation mode, compressive stress is expected due to the exothermal process caused while in SOEC mode, tensile stress over the stack components is expected due to the endothermal process. Dynamic current modelling shows that in SOEC mode, with the increase of current density, the tensile stress firstly increases and decreases afterwards, highest tensile stress taking place at -0.5A/cm^2. Reducing the external compression force during stack testing may help to reduce the tensile stress on the stack component. Following this helpful uptake, some modifications on the stack testing procedure have been discussed with [**ELCOGEN**], such as increasing the current ramping steps. This will enable to minimize the temperature change and therefore lowering the stress on the stack and will be implemented in the next stack test in the C2FUEL project. Results will be reported in **Deliverable D2.9.** Furthermore 0D modelling reveals a large uneven distribution of current density especially when operated at high current densities, which is in good agreement with experimental microstructure analysis, showing more severe microstructure change at the steam inlet of the fuel electrode than outlet [18]. Based on this work, the recommendation is to decrease the operating current density of the electrolyser. However, in the frame of the demonstrator, it is already fixed to reach the objective of 1 Nm^3/h of H_2 production. This valuable information will therefore be exploited in the techno-economic analysis, where a trade-off between efficiency and durability of the stack will be discussed.

8 References

[1] Li, A., Song, C., & Lin, Z. (2017). A multiphysics fully coupled modeling tool for the design and operation analysis of planar solid oxide fuel cell stacks. Applied energy, 190, 1234-1244.

[2] Navasa, M., Miao, X. Y., & Frandsen, H. L. (2019). A fully-homogenized multiphysics model for a reversible solid oxide cell stack. International Journal of Hydrogen Energy, 44(41), 23330-23347.

[3] Rizvandi, O. B., Miao, X. Y., & Frandsen, H. L. (2021). Multi-scale modeling of degradation of full solid oxide fuel cell stacks. International Journal of Hydrogen Energy, 46, 27709-27730.

[4] Miao, X. Y., Rizvandi, O. B., Navasa, M., & Frandsen, H. L. (2021). Modelling of local mechanical failures in solid oxide cell stacks. Applied Energy, 293, 116901.

[5] Nishida, R. T., Beale, S. B., & Pharoah, J. G. (2016). Comprehensive computational fluid dynamics model of solid oxide fuel cell stacks. International Journal of Hydrogen Energy, 41(45), 20592-20605.

[6] Kvesić, M., Reimer, U., Froning, D., Lüke, L., Lehnert, W., & Stolten, D. (2012). 3D modeling of a 200 cm2 HT-PEFC short stack. International journal of hydrogen energy, 37(3), 2430-2439.

[7] Nishida, R. T., Beale, S. B., Pharoah, J. G., de Haart, L. G. J., & Blum, L. (2018). Three-dimensional computational fluid dynamics modelling and experimental validation of the Jülich Mark-F solid oxide fuel cell stack. Journal of Power Sources, 373, 203-210.

[8] Kawada, T., Sakai, N., Yokokawa, H., Dokiya, M., Mori, M., & Iwata, T. (1990). Characteristics of slurry-coated nickel zirconia cermet anodes for solid oxide fuel cells. Journal of the Electrochemical Society, 137(10), 3042.

[9] Nagata, S., Momma, A., Kato, T., & Kasuga, Y. (2001). Numerical analysis of output characteristics of tubular SOFC with internal reformer. Journal of Power Sources, 101(1), 60-71.

[10] Suzue, Y., Shikazono, N., & Kasagi, N. (2008). Micro modeling of solid oxide fuel cell anode based on stochastic reconstruction. Journal of Power Sources, 184(1), 52-59.

[11] Miyoshi, K., Miyamae, T., Iwai, H., Saito, M., Kishimoto, M., & Yoshida, H. (2016). Exchange current model for (La0. 8Sr0. 2) 0.95 MnO3 (LSM) porous cathode for solid oxide fuel cells. Journal of Power Sources, 315, 63-69.

[12] Leonide, A., Apel, Y., & Ivers-Tiffee, E. (2009). SOFC modeling and parameter identification by means of impedance spectroscopy. ECS Transactions, 19(20), 81.

[13] Kong, W., Li, J., Liu, S., & Lin, Z. (2012). The influence of interconnect ribs on the performance of planar solid oxide fuel cell and formulae for optimal rib sizes. Journal of Power Sources, 204, 106-115.

[14] Navasa, M., Graves, C., Chatzichristodoulou, C., Skafte, T. L., Sundén, B., & Frandsen, H. L. (2018). A three dimensional multiphysics model of a solid oxide electrochemical cell: A tool for understanding degradation. International Journal of Hydrogen Energy, 43(27), 11913-11931.

[15] Ni, M., Leung, M. K., & Leung, D. Y. (2007). Parametric study of solid oxide steam electrolyzer for hydrogen production. International Journal of Hydrogen Energy, 32(13), 2305-2313.

[16] Liu, S., Kong, W., & Lin, Z. (2009). Three-dimensional modeling of planar solid oxide fuel cells and the rib design optimization. Journal of Power Sources, 194(2), 854-863.

[17] Bernadet, L., Gousseau, G., Chatroux, A., Laurencin, J., Mauvy, F., & Reytier, M. (2015). Influence of pressure on solid oxide electrolysis cells investigated by experimental and modeling approach. international journal of hydrogen energy, 40(38), 12918-12928.

[18] Sun, X., Hendriksen, P.V., Mogensen, M, B., Chen, M. (2019). Degradation in Solid Oxide Electrolysis Cells During Long Term Testing. Fuel Cells, 19:740–7.